51st AIAA Aerospace Sciences Meeting including the New Horizons Forum and Aerospace Exposition
07 - 10 January 2013, Grapevine (Dallas/Ft. Worth Region), Texas
AIAA 2013-0827

The stabilization of a Mach 10 boundary layer using regular porous coating

Xiaowen Wang* and Xiaolin Zhong #1
Mechanical and Aerospace Engineering Department
University of California, Los Angeles, CA 90095

Abstract

The stabilization of hypersonic boundary layers using porous coatings has been studied by theoretical analyses, experiments, and numerical simulations in the past decade. It was found that porous coating stabilizes Mack's second mode and destabilizes Mack's first mode. However, no work has been reported about the thermochemical non-equilibrium effects of hypersonic flows on porous coating stabilization efficiency. Our previous results show that thermochemical non-equilibrium of hypersonic flows may affect the stabilization efficiency of regular coating. Therefore, numerical simulations for perfect gas flow may not be enough. In this paper, we conduct numerical simulations on the stabilization of a Mach 10 boundary layer using regular porous coating. The effects of thermochemical non-equilibrium flow including internal energy excitations, translation-vibration energy relaxation, and chemical reactions among different species are considered. Three types of steady base flow for perfect gas, thermal equilibrium and chemical non-equilibrium gas, and thermochemical non-equilibrium gas are first investigated. The stability characteristics of the Mach 10 boundary layer are studied by the linear stability theory based on perfect gas solution. Response of the boundary layer to single-frequency wall blowing-suction is studied by six cases of unsteady simulations for perfect gas. The preliminary results show regular porous coating has a significant effect on boundary-layer instability.

1. Introduction

The performance of hypersonic transportation vehicles and re-entry vehicles and the design of their thermal protection systems are significantly affected by the laminar-turbulent transition of boundary-layer flows over vehicle surfaces, because a turbulent boundary layer generates much higher drag and surface heating than a laminar one. Transition can have a first-order impact on the lift, drag, stability, control, and heat transfer properties of the vehicles [1]. Transition control to maintain laminar boundary-layer flows or delay transition can result in lower drag, lower surface heating, and higher fuel efficiency.

In order to predict and control boundary-layer transition, extensive studies have been carried out focusing on transition mechanisms [2]. It has been demonstrated that the transition of external shear flows, including boundary layers, strongly depends on the amplitude of environmental disturbance [3]. Figure 1 schematically shows paths of external shear flow transition. For small amplitude disturbance, the transition of a boundary layer over a smooth surface generally consists of the following three stages: 1. receptivity process during which environmental disturbances enter the boundary layer and excite boundary-layer waves. 2. Modal growth of unstable boundary-layer waves which can be obtained by solving the eigenvalue problem of the homogeneous linearized stability equations. 3. Breakdown to turbulence caused by non-linear

* Research Associate, Mechanical and Aerospace Engineering Department, UCLA, AIAA Senior Member
# Professor, Mechanical and Aerospace Engineering Department, UCLA, AIAA Associate Fellow

secondary instabilities and three-dimensional effects when the unstable waves reach certain amplitude. This three-stage-transition mechanism is path 1 as shown in Fig. 1. With the disturbance amplitude increasing, transient growth, arising through the non-orthogonal nature of the Orr-Sommerfeld eigenfunctions and the Squire eigenfunctions, becomes important. Weak transient growth provides higher initial amplitude for modal growth (path 2) whereas strong transient growth can lead to secondary instabilities and breakdown to turbulence right after the receptivity process (path 3). In the current study, only small amplitude disturbances are considered. Regular porous coating is used to stabilize the boundary layer by attenuating modal growth. The mechanism of porous coating's absorbing energy from Mack's second mode is similar to that of car exhaust muffler's reducing noise emitted by the exhaust of an internal combustion engine.

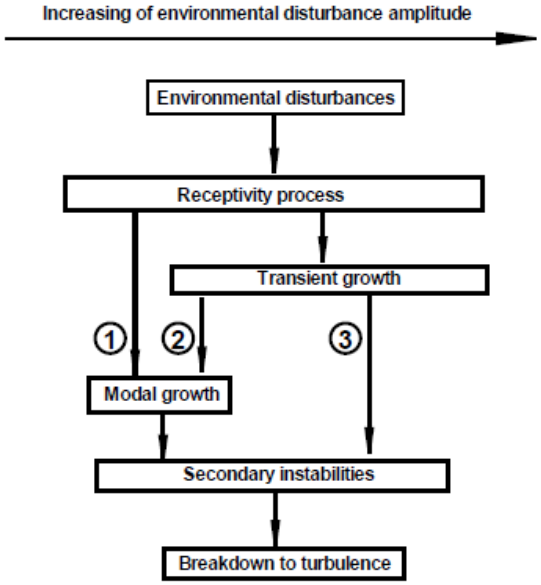

Fig. 1. Paths of external shear flow transition with respect to the amplitude of environmenta disturbance[3].

In the past decade, passive control of boundary-layer transition by using porous coating has been studied by theoretical analyses [4-7], experiments [8-13], and numerical simulations [14-16]. It was found that porous coating stabilizes Mack's second mode and destabilizes Mack's first mode. Recently, Wang and Zhong [17] studied the stabilization of a Mach 5.92 flat-plate boundary layer by using local sections of felt-metal porous coating. Artificial disturbances corresponding to a single boundary-layer wave were introduced near the leading edge. It was found that disturbances of mode S are destabilized or stabilized when porous coating is located upstream or downstream of the synchronization point. For felt-metal porous coating, the destabilization of Mack's first mode is significant. More details of previous research in this area are summarized in the paper presented on the Seventh International Conference on Computational Fluid Dynamics [18].

However, no work has been reported about the thermochemical non-equilibrium effects of hypersonic flows on the stabilization efficiency of porous coating. In a previous study, we analyzed the effect of the phase angle of regular coating admittance [19]. Numerical simulations are carried out on one regular porous coating at the given parameters (phase angle > π) and one "artificial" porous coatings with zero imaginary part of admittance (phase angle = π). Figure 2 shows the change of phase angle with the peak of velocity perturbation moving upstream. Figure 3 compares the pressure perturbation amplitudes of the two regular porous coatings, together with the spatial development of mode S along solid wall. The figure shows that pressure

perturbation amplitude decreases for a smaller phase angle of admittance. Since the synchronization point is located around x = 0.33 m, the results indicate that Mack's first-mode destabilization is weakened by the decrease of admittance phase angle. However, the second mode stabilization is approximately unchanged because pressure perturbations of the two porous coatings increase proportionally after the synchronization point.

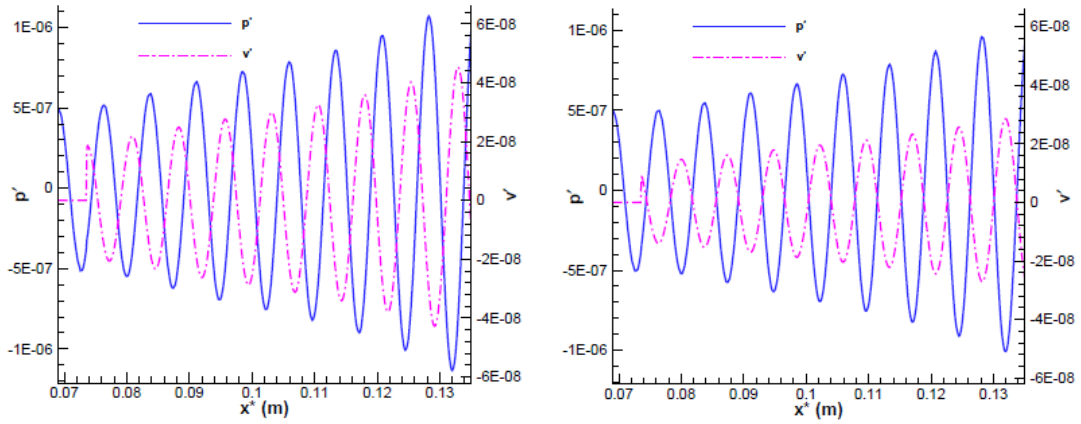

(a) at the given parameters *(b) zero imaginary part of admittance*

Fig. 2. Instantaneous pressure and velocity perturbations along the flat plate with regular porous coating.

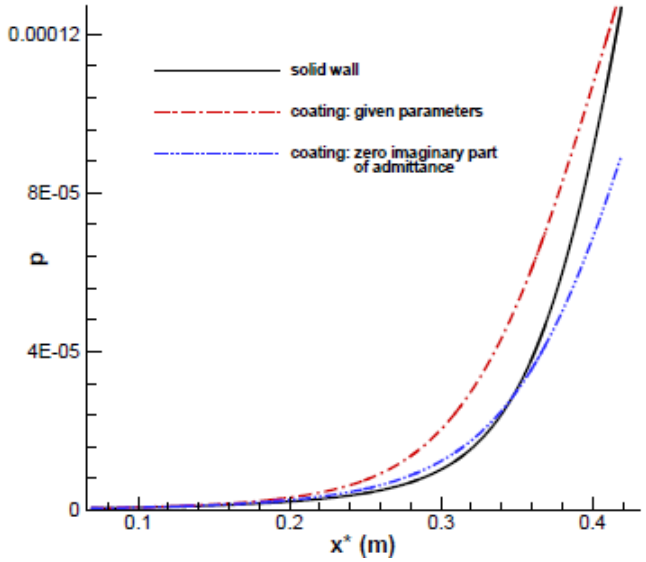

Fig. 3. Comparison of pressure perturbation amplitudes of the two regular porous coatings.

We further analyzed the admittance of porous coating and its dependent variables. According to the model of regular coating, the admittance phase angle depends on three parameters: thickness, pore size, and ratio of specific heat. Figure 4 plots the phase angle of admittance versus the three parameters, respectively, with the other parameters of porous coating unchanging. Figure 4(c) shows that admittance phase angle decreases as the ratio of specific heat increases, which indicates the effects of thermochemical non-equilibrium flow will lead to weaker destabilization of Mack's first mode.

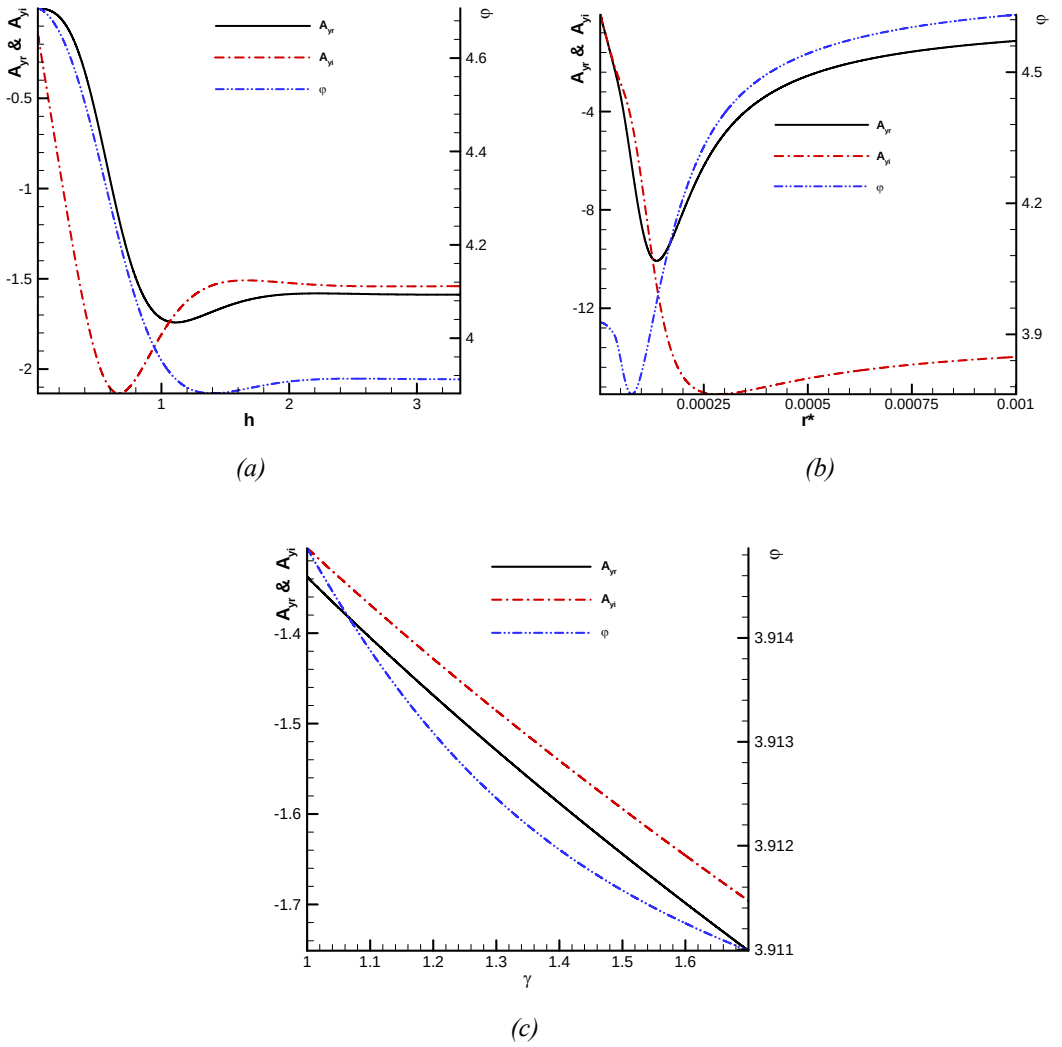

Fig. 4. Phase angle of regular porous coating admittance versus its dependent varialbes: (a) thickness, (b) pore size, and (c) the ratio of specific heat.

We have also studied a Mach 12.56 flow over a blunted wedge of a half angle of 20 degree [18]. The effects of different viscosity are taken into account by conducting three cases of numerical simulation: 1) perfect gas flow with Sutherland's law, 2) perfect gas flow with the transport properties being calculated from collision cross-section area, and 3) thermochemical non-equilibrium flow with the transport properties being calculated from collision cross-section area. Figure 5 shows the streamwise velocity profile across the boundary layer at the intersection of the blunted leading edge and the wedge. The boundary layer of case 2 is a little bit thicker than that of case 1, because the viscosity coefficent of perfect gas flow calculated from collision cross-section area is lower than that calculated from Sutherland's law. In addition, the boundary layer of case 3 is thinner than that of case 2. The results show that the effects of thermochemical non-equilibrium flow and viscosity models can be successfully separated by conducting the three cases of numerical simulations.

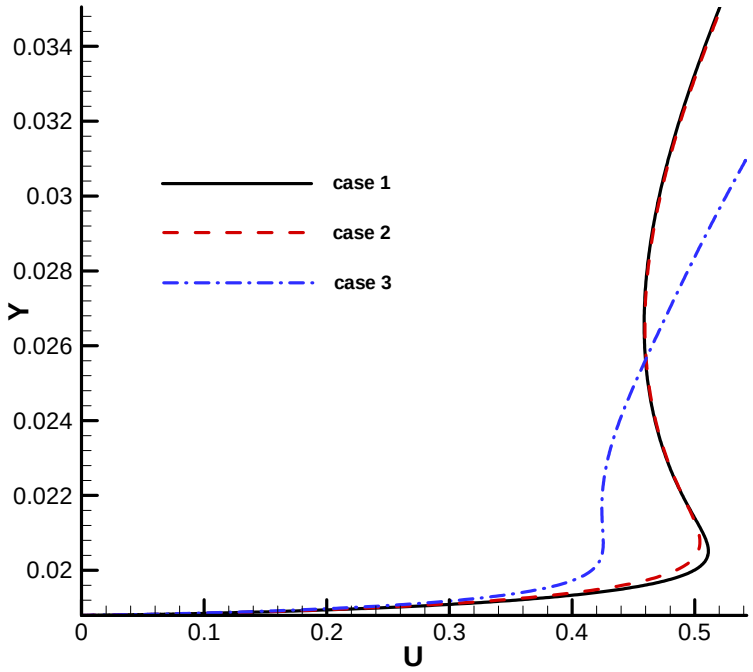

Fig. 5. Comparison of streamwise velocity profile across the boundary layer.

These results indicate that thermochemical non-equilibrium effects may affect the stabilization of hypersonic boundary layers using regular porous coating in two aspects: (1) change of the ratio of specific heat, and (2) change of viscosity coefficient and stability characteristics. In this paper, we conduct numerical simulations on the stabilization of a Mach 10 boundary layer over a flat plate using regular porous coating. The effects of thermochemical non-equilibrium flow including internal energy excitations, translation-vibration energy relaxation, and chemical reactions among different species are considered. Compared to the Mach 12.56 flow over a blunted wedge in [18], the current flow has stronger dissociations and more significant Mack's second mode. Three types of steady base flow for perfect gas, thermal equilibrium and chemical non-equilibrium gas, and thermochemical non-equilibrium gas are first investigated. The stability characteristics of the Mach 10 boundary layer are studied by the linear stability theory based on perfect gas solution. Response of the boundary layer to single-frequency wall blowing-suction is studied by six cases of unsteady simulations for perfect gas. The preliminary results show regular porous coating has a significant effect on boundary-layer instability. More unsteady simulations on the passive control of hypersonic non-equilibrium boundary-layer transition using regular porous coating are currently ongoing.

2. Governing Equations and Numerical Methods

2.1 Governing equations of perfect gas flow

The governing equations of perfect gas flow are written in the following conservation-law form in the Cartesian coordinates,

$$\frac{\partial U}{\partial t}+\frac{\partial F_j}{\partial x_j}+\frac{\partial F_{vj}}{\partial x_j}=0 \tag{1}$$

where U, F_j and F_{vj} are the vectors of conservative variables, convective and viscous flux in the direction of jth coordinate, respectively, i.e.,

$$U=\{\rho,\rho u_1,\rho u_2,\rho u_3,e\} \tag{2}$$

$$F_j=\begin{Bmatrix}\rho u_j\\ \rho u_1u_j+P\delta_{1j}\\ \rho u_2u_j+P\delta_{1j}\\ \rho u_3u_j+P\delta_{1j}\\ (e+p)u_j\end{Bmatrix},\ F_{vj}=\begin{Bmatrix}0\\ -\tau_{1j}\\ -\tau_{2j}\\ -\tau_{3j}\\ -\tau_{jk}u_k+q_j\end{Bmatrix} \tag{3}$$

For the simulation of perfect gas flow, the following equations are needed.

$$P=\rho RT \tag{4}$$

$$e=\rho(c_vT+\frac{1}{2}u_ku_k) \tag{5}$$

$$\tau_{ij}=\mu(\frac{\partial u_i}{\partial x_j}+\frac{\partial u_j}{\partial x_i})+\delta_{ij}\lambda\frac{\partial u_k}{\partial x_k} \tag{6}$$

$$q_j=-k\frac{\partial T}{\partial x_j} \tag{7}$$

where R is the gas constant. The specific heat c_v is a constant determined by a given ratio of specific heats γ. The viscosity coefficient μ is calculated by Sutherland's law,

$$\mu=\mu_r\left(\frac{T}{T_0}\right)^{3/2}\frac{T_0+T_s}{T+T_s} \tag{8}$$

For air, $\mu_r=1.7894\times10^{-5}$ Ns/m^2, $T_0=288.0$ K, $T_s=110.33$ K, and $\lambda=-2\mu/3$. The heat conductivity coefficient k is computed by a given Prandtl number.

2.2 Governing equations of thermochemical non-equilibrium flow

The governing equations of thermochemical non-equilibrium flow based on 5-species air chemistry are Navier-Stokes equations with source terms (no radiation). Specifically, they consist of the flowing equations,

$$\frac{\partial\rho_s}{\partial t}+\frac{\partial}{\partial x_j}(\rho_su_j)-\frac{\partial}{\partial x_j}(\rho D_s\frac{\partial y_s}{\partial x_j})=\omega_s \tag{9}$$

$$\frac{\partial}{\partial t}(\rho u_i)+\frac{\partial}{\partial x_j}(\rho u_iu_j+p\delta_{ij})-\frac{\partial}{\partial x_j}\left[\mu\left(\frac{\partial u_i}{\partial x_j}+\frac{\partial u_j}{\partial x_i}\right)-\frac{2}{3}\mu\frac{\partial u_k}{\partial x_k}\delta_{ij}\right]=0 \tag{10}$$

$$\frac{\partial\rho E}{\partial t}+\frac{\partial}{\partial x_j}(\rho Hu_j)-\frac{\partial}{\partial x_j}\left[u_i\mu\left(\frac{\partial u_i}{\partial x_j}+\frac{\partial u_j}{\partial x_i}\right)-\frac{2}{3}u_i\mu\frac{\partial u_k}{\partial x_k}\delta_{ij}\right]$$

$$-\frac{\partial}{\partial x_j}\left(\rho\sum_{s=1}^{5}h_s D_s\frac{\partial y_s}{\partial x_j}\right)-\frac{\partial}{\partial x_j}\left(K\frac{\partial T}{\partial x_j}+K_V\frac{\partial T_V}{\partial x_j}\right)=0 \tag{11}$$

$$\frac{\partial \rho E_V}{\partial t}+\frac{\partial}{\partial x_j}(\rho E_V u_j)-\frac{\partial}{\partial x_j}(\rho\sum_{s=1}^{5}e_{V,s}D_s\frac{\partial y_s}{\partial x_j})-\frac{\partial}{\partial x_j}\left(K_V\frac{\partial T_V}{\partial x_j}\right)=\sum_{s=1}^{3}Q_{T-V,s}+\sum_{s=1}^{5}\omega_s e_{V,s} \tag{12}$$

where,

$$\rho=\sum_{s=1}^{5}\rho_s \qquad u_j=\frac{1}{\rho}\sum_{s=1}^{5}\rho_s u_{sj} \qquad y_s=\frac{(\rho_s/M_s)}{\sum_{i=1}^{5}(\rho_i/M_i)}$$

$$p=\sum_{s=1}^{5}p_s=\sum_{s=1}^{5}\frac{\rho_s\bar{R}T}{M_s} \qquad E=\frac{u_i u_i}{2}+\sum_{s=1}^{5}\frac{\rho_s e_s}{\rho} \qquad H=E+\frac{p}{\rho}$$

$\bar{R}$ is the universal gas constant. The formulas of species diffusion coefficient D_s, viscosity μ, heat conductivities K and K_V, species internal energy e_s and $e_{V,s}$, specific vibration energy E_V, and source terms depends on the models of thermochemical non-equilibrium flow.

The corresponding matrix form of governing equations is as follows,

$$\frac{\partial U}{\partial t}+\frac{\partial F_j}{\partial x_j}+\frac{\partial G_j}{\partial x_j}=S \tag{13}$$

where the vector of conservative variables has ten components,

$$U=\left(\rho_1,\rho_2,\ldots,\rho_5,\rho u,\rho v,\rho w,\rho E,\rho e_V\right)^{\mathrm{T}} \tag{14}$$

The inviscid and viscous flux in the direction of jth coordinate, F_j and G_j, and the source term S are given below.

$$F_j=\begin{pmatrix}\rho_1 u_j\\ \rho_2 u_j\\ \vdots\\ \rho_5 u_j\\ \rho u u_j+p\delta_{1j}\\ \rho v u_j+p\delta_{2j}\\ \rho w u_j+p\delta_{3j}\\ \rho H u_j\\ \rho e_V u_j\end{pmatrix},\ G_j=\begin{pmatrix}\rho_1 v_{1j}\\ \rho_2 v_{2j}\\ \vdots\\ \rho_5 v_{5j}\\ -\tau_{1j}\\ -\tau_{2j}\\ -\tau_{3j}\\ -u_i\tau_{ij}+q_j+q_{Vj}+\sum_{s=1}^{5}\rho_s h_s v_{sj}\\ q_{Vj}+\sum_{s=1}^{5}\rho_s e_{V,s}v_{sj}\end{pmatrix},\ S=\begin{pmatrix}\omega_1\\ \omega_2\\ \vdots\\ \omega_5\\ 0\\ 0\\ 0\\ 0\\ \sum_{s=1}^{3}(Q_{T-V,s}+\omega_s e_{V,s})\end{pmatrix} \tag{15}$$

In above equations, $v_{sj}=u_{sj}-u_j$ is diffusion velocity of species s.

$$v_{sj}=-\frac{\rho D_s}{\rho_s}\frac{\partial y_s}{\partial x_j} \tag{16}$$

The model of vibration and electron energy used in Hash et al.'s paper [20] are implemented in the code. Specific total enthalpy of species and specific heat in constant pressure of species are defined as,

$$h_s = c_{vs}T + \frac{p_s}{\rho_s} + e_{V,s} + h_s^0 \tag{17}$$

$$c_p^s = c_v^s + \frac{\bar{R}}{M_s} + c_V^s \tag{18}$$

where h_s^0 is the generation enthalpy of species. The variables on the right hand side of equations (17) and (18) are calculated from the following formula,

$$e_{V,s} = (e_V + e_{els}) = \frac{\bar{R}}{M_s}\left(\sum_{s=1}^{3}\frac{\theta_{vs}}{e^{\theta_{vs}/T_V}-1} + \sum_{s=1}^{5}\frac{\sum_{i=1}^{\infty} g_{i,s}\theta_{el,i,s}\exp(-\theta_{el,i,s}/T_V)}{\sum_{i=0}^{\infty} g_{i,s}\exp(-\theta_{el,i,s}/T_V)}\right) \tag{19}$$

$$c_v^s = c_{vtr,s} + c_{vrot,s} \tag{20}$$

$$c_{vtr,s} = \frac{3\bar{R}}{2M_s} \tag{21}$$

$$c_{vrot,s} = \begin{cases} \dfrac{\bar{R}}{M_s} & (s = 1,3) \\ 0 & (otherwise) \end{cases} \tag{22}$$

$$c_V^s = \frac{\bar{R}}{M_s}\left\{\frac{(\theta_{vs}/T_V)^2 e^{\theta_{vs}/T_V}}{\left(e^{\theta_{vs}/T_V}-1\right)^2} + \frac{\left[\sum_{i=1}^{\infty} g_{i,s}\left(\theta_{el,i,s}/T_V\right)^2\exp(-\theta_{el,i,s}/T_V)\right]}{\sum_{i=0}^{\infty} g_{i,s}\exp(-\theta_{el,i,s}/T_V)} - \frac{\left[\sum_{i=1}^{\infty} g_{i,s}\theta_{el,i,s}\exp(-\theta_{el,i,s}/T_V)\right]\left[\sum_{i=0}^{\infty} g_{i,s}\left(\theta_{el,i,s}/T_V^2\right)\exp(-\theta_{el,i,s}/T_V)\right]}{\left(\sum_{i=0}^{\infty} g_{i,s}\exp(-\theta_{el,i,s}/T_V)\right)^2}\right\} \tag{23}$$

For the 5-species air, the related parameters used in the models of vibration and electron energy are listed in Table 1 and Table 2. Compared to other models [21, 22], the current models have the advantage of directly applicable to unlimited high temperatures.

Table 1. Parameters used vibration energy model

Species	h_s^0 (J/kg)	M_s (g)	θ_{vs} (K)
N2	0	28	3395
O2	0	32	2239
NO	2.996123e6	30	2817
N	3.362161e7	14	-
O	1.543119e7	16	-

Table 2. Electronic energy states for 5-species air

Species	Θ (K)	g	Species	Θ (K)	g	Species	ΘO (K)	g
N2	0	1	O2	1.13916e4	2	NO	8.88608e4	4
N2	7.22316e4	3	O2	1.89847e4	1	NO	8.98176e4	4
N2	8.57786e4	6	O2	4.75597e4	1	NO	8.98845e4	2
N2	8.60503e4	6	O2	4.99124e4	6	NO	9.04270e4	2
N2	9.53512e4	3	O2	5.09227e4	3	NO	9.06428e4	2
N2	9.80564e4	1	O2	7.18986e4	3	NO	9.11176e4	4
N2	9.96827e4	2	NO	0	4	N	0	4
N2	1.04898e5	2	NO	5.46735e4	8	N	2.76647e4	10
N2	1.11649e5	5	NO	6.31714e4	2	N	4.14931e4	6
N2	1.22584e5	1	NO	6.59945e4	4	O	0	5
N2	1.24886e5	6	NO	6.90612e4	4	O	2.27708e2	3
N2	1.28248e5	6	NO	7.0500e4	4	O	3.26569e2	1
N2	1.33806e5	10	NO	7.49106e4	4	O	2.28303e4	5
N2	1.40430e5	6	NO	7.62888e4	2	O	4.86199e4	1
N2	1.50496e5	6	NO	8.67619e4	4			
O2	0	3	NO	8.71443e4	2			

For the 5-species air, a more complex model of thermal properties is applied [23]. Thermal properties are calculated as follows,

$$\mu = \sum_s \frac{m_s \gamma_s}{\sum_r \gamma_r \Delta_{sr}^{(2)}(T)} \quad \textbf{(g/cm-sec)} \tag{24}$$

$$K_T = \frac{15}{4} k \sum_s \frac{\gamma_s}{\sum_r a_{sr} \gamma_r \Delta_{sr}^{(2)}(T)} \quad \textbf{(J/cm-sec-K)} \tag{25}$$

In above equation, $a_{sr} = 1 + \frac{\left[1-(m_s/m_r)\right]\left[0.45-2.54(m_s/m_r)\right]}{\left[1+(m_s/m_r)\right]^2}$.

$$K_R = k \sum_{s=1,2,3} \frac{\gamma_s}{\sum_r \gamma_r \Delta_{sr}^{(1)}(T)} \quad \textbf{(J/cm-sec-K)} \tag{26}$$

$$K_{V-E} = k \frac{C_{V,V}}{R} \sum_{s=1}^{5} \frac{\gamma_s}{\sum_r \gamma_r \Delta_{sr}^{(1)}(T)} \quad \textbf{(J/cm-sec-K)} \tag{27}$$

To calculate viscosity and heat conductivity, the collision terms are as follows,

$$\Delta_{sr}^{(1)}(T)=\frac{8}{3}\left[\frac{2m_s m_r}{\pi RT(m_s+m_r)}\right]^{1/2}10^{-20}\pi\Omega_{sr}^{(1,1)}(T)\ \textbf{(cm-sec)}$$

$$\Delta_{sr}^{(2)}(T)=\frac{16}{3}\left[\frac{2m_s m_r}{\pi RT(m_s+m_r)}\right]^{1/2}10^{-20}\pi\Omega_{sr}^{(2,2)}(T)\ \textbf{(cm-sec)}$$

Collision integrals involving neutrals (Non-Coulombic collision integrals) are

$$\pi\Omega_{sr}^{(l,j)}(T)=DT^{\left[A(\ln T)^2+B\ln T+C\right]}\ (\overset{0}{\mathrm{A}}^2) \tag{28}$$

Species diffusion coefficients are defined as,

$$D_s=\frac{(1-y_s)}{\sum_{r\neq s}(y_r/D_{sr})} \tag{29}$$

For binary diffusion between heavy particles, $D_{sr}=\dfrac{kT}{p\Delta_{sr}^{(1)}(T)}$. The heat conductivities K and K_V in governing equations are calculated as,

$$K=K_T+K_R \tag{30}$$

$$K_V=K_{V-E} \tag{31}$$

For chemical non-equilibrium, five reactions are considered for the five species air, i.e.,

$$\left.\begin{aligned} N_2+M&=2N+M\\ O_2+M&=2O+M\\ NO+M&=N+O+M\\ N_2+O&=NO+N\\ NO+O&=O_2+N \end{aligned}\right\} \tag{32}$$

Correspondingly, the reaction rates are calculated as follows,

$$\left\{\begin{aligned} R_1&=\sum_m\left[-k_{f_1m}\frac{\rho_{N_2}}{M_{N_2}}\frac{\rho_m}{M_m}+k_{b_1m}\frac{\rho_N}{M_N}\frac{\rho_N}{M_N}\frac{\rho_m}{M_m}\right]\\ R_2&=\sum_m\left[-k_{f_2m}\frac{\rho_{O_2}}{M_{O_2}}\frac{\rho_m}{M_m}+k_{b_2m}\frac{\rho_O}{M_O}\frac{\rho_O}{M_O}\frac{\rho_m}{M_m}\right]\\ R_3&=\sum_m\left[-k_{f_3m}\frac{\rho_{NO}}{M_{NO}}\frac{\rho_m}{M_m}+k_{b_3m}\frac{\rho_N}{M_N}\frac{\rho_O}{M_O}\frac{\rho_m}{M_m}\right]\\ R_4&=-k_{f_4}\frac{\rho_{N_2}}{M_{N_2}}\frac{\rho_O}{M_O}+k_{b_4}\frac{\rho_{NO}}{M_{NO}}\frac{\rho_N}{M_N}\\ R_5&=-k_{f_5}\frac{\rho_{NO}}{M_{NO}}\frac{\rho_O}{M_O}+k_{b_5}\frac{\rho_{O_2}}{M_{O_2}}\frac{\rho_N}{M_N} \end{aligned}\right. \tag{33}$$

Finally, the source terms are as follows,

$$\begin{cases} \omega_{N_2} = M_{N_2}(R_1 + R_4) \\ \omega_{O_2} = M_{O_2}(R_2 - R_5) \\ \omega_{NO} = M_{NO}(R_3 - R_4 + R_5) \\ \omega_N = M_N(-2R_1 - R_3 - R_4 - R_5) \\ \omega_O = M_O(-2R_2 - R_3 + R_4 + R_5) \end{cases} \tag{34}$$

The forward and backward reaction rate coefficients have the form of

$$k_f\left(\overline{T}\right) = C_f \overline{T}^{\eta_f} \exp\left(-\theta_f / \overline{T}\right) \tag{35}$$

$$k_b\left(T\right) = \frac{k_f(T)}{k_{eq}(T)} \tag{36}$$

For dissociation reactions, $\overline{T} = \sqrt{TT_V}$. For the other reactions, the control temperature is $\overline{T} = T$. The equilibrium constant is obtained using the curve fits of Park [24], i.e.,

$$k_{eq} = \exp(a_1 z^{-1} + a_2 + a_3 \ln z + a_4 z + a_5 z^2) \tag{37}$$

In two temperature model, energy relaxation only happens between translation energy and vibration & electron energy, which can be expressed as

$$Q_{T-v,s} = \rho_s \frac{e_{vs}^*(T) - e_{vs}}{\tau_{vs}} \tag{38}$$

where, $e_{vs}^*(T)$ is the vibration energy per unit mass of species s evaluated at the local translational temperature.

$$\tau_{vs} = \left\langle \tau_{s,L-T} \right\rangle + \tau_{cs} = \frac{\sum_r y_r}{\sum_r y_r / \tau_{sr,L-T}} + \frac{1}{a_s \sigma_v N_s} \qquad (a_s = \sqrt{\frac{8\overline{R}T}{\pi M_s}})$$

$$\tau_{sr,L-T} = \frac{1}{p} \exp\left[A_{sr}\left(T^{-1/3} - 0.015\mu_{sr}^{1/4}\right) - 18.42 \right] \text{ (p in atm)}$$

$$A_r = 1.16 \times 10^{-3} \mu_{sr}^{1/2} \theta_{vs}^{4/3} \qquad \mu_{sr} = M_s M_r / (M_s + M_r)$$

$$S_s = 3.5 \exp\left(-\theta_s / T_{shk} \right) \qquad \sigma_v = 10^{-21} \left(50{,}000 / T \right)^2$$

Here, θ_s is a defined characteristic temperature listed in Table 1.

2.3 Coordinate transform

The flow solver uses structured grids. The following grid transform is applied in the computational domain,

$$\begin{cases} x = x(\xi, \eta, \zeta, \tau) \\ y = y(\xi, \eta, \zeta, \tau) \\ z = z(\xi, \eta, \zeta, \tau) \\ t = \tau \end{cases} \Leftrightarrow \begin{cases} \xi = \xi(x, y, z, t) \\ \eta = \eta(x, y, z, t) \\ \zeta = \zeta(x, y, z, t) \\ \tau = t \end{cases} \tag{39}$$

The Jacobian of the above coordinate transform is,

$$J = \begin{vmatrix} x_\xi & y_\xi & z_\xi & 0 \\ x_\eta & y_\eta & z_\eta & 0 \\ x_\zeta & y_\zeta & z_\zeta & 0 \\ x_\tau & y_\tau & z_\tau & 1 \end{vmatrix} \tag{40}$$

With the transform, the governing equations in (ξ, η, ζ, τ) coordinate system are written as

$$\frac{\partial (JU)}{\partial \tau} + \frac{\partial \tilde{F}_1}{\partial \xi} + \frac{\partial \tilde{F}_2}{\partial \eta} + \frac{\partial \tilde{F}_3}{\partial \zeta} + \frac{\partial \tilde{G}_1}{\partial \xi} + \frac{\partial \tilde{G}_2}{\partial \eta} + \frac{\partial \tilde{G}_3}{\partial \zeta} = JS \tag{41}$$

where

$$\begin{aligned}
\tilde{F}_1 &= J\xi_x F_1 + J\xi_y F_2 + J\xi_z F_3 + JU\xi_t \\
\tilde{F}_2 &= J\eta_x F_1 + J\eta_y F_2 + J\eta_z F_3 + JU\eta_t \\
\tilde{F}_3 &= J\zeta_x F_1 + J\zeta_y F_2 + J\zeta_z F_3 + JU\zeta_t \\
\tilde{G}_1 &= J\xi_x G_1 + J\xi_y G_2 + J\xi_z G_3 \\
\tilde{G}_2 &= J\eta_x G_1 + J\eta_y G_2 + J\eta_z G_3 \\
\tilde{G}_3 &= J\zeta_x G_1 + J\zeta_y G_2 + J\zeta_z G_3
\end{aligned}$$

2.4 Numerical method

The governing equations are solved by the fifth-order shock-fitting method of Zhong [25]. For the thermochemical non-equilibrium system (13) in the direction, $\mathrm{k} = (k_1, k_2, k_3)$, the corresponding inviscid flux term is

$$\mathrm{F} = \begin{pmatrix} \rho_1 \mathrm{k\,u} \\ \rho_2 \mathrm{k\,u} \\ \rho_3 \mathrm{k\,u} \\ \rho_4 \mathrm{k\,u} \\ \rho_5 \mathrm{k\,u} \\ \rho u \mathrm{k\,u} + p k_1 \\ \rho v \mathrm{k\,u} + p k_2 \\ \rho w \mathrm{k\,u} + p k_3 \\ \rho H \mathrm{k\,u} \\ \rho E_V \mathrm{k\,u} \end{pmatrix} \tag{42}$$

Hence the Jacobian of flux is defined as,

$$\mathrm{A} = \frac{\partial \mathrm{F}}{\partial \mathrm{U}} = L\Lambda R \tag{43}$$

$$A=|\mathrm{k}|\begin{bmatrix}\tilde{U}(\delta_{sr}-c_s) & c_s n_x & c_s n_y & c_s n_z & 0 & 0\\ \tilde{\gamma}_r n_x-\tilde{U}u & -\beta u n_x+u n_x+\tilde{U} & -\beta v n_x+u n_y & -\beta w n_x+u n_z & \beta n_x & \phi n_x\\ \tilde{\gamma}_r n_y-\tilde{U}v & -\beta u n_y+v n_x & -\beta v n_y+v n_y+\tilde{U} & -\beta w n_y+v n_z & \beta n_y & \phi n_y\\ \tilde{\gamma}_r n_z-\tilde{U}w & -\beta u n_z+w n_x & -\beta v n_z+w n_y & -\beta w n_z+w n_z+\tilde{U} & \beta n_z & \phi n_z\\ \tilde{\gamma}_r\tilde{U}-\tilde{U}H & -\beta u\tilde{U}+H n_x & -\beta v\tilde{U}+H n_y & -\beta w\tilde{U}+H n_z & \beta\tilde{U}+\tilde{U} & \phi\tilde{U}\\ -\tilde{U}e_V & e_V n_x & e_V n_y & e_V n_z & 0 & \tilde{U}\end{bmatrix}$$

$$R=\begin{bmatrix}a^2\delta_{sr}-c_s\tilde{\gamma}_r & \beta u c_s & \beta v c_s & \beta w c_s & -\beta c_s & -\phi c_s\\ -\tilde{V} & l_x & l_y & l_z & 0 & 0\\ -\tilde{W} & m_x & m_y & m_z & 0 & 0\\ \tilde{\gamma}_r-\tilde{U}a & a n_x-\beta u & a n_y-\beta v & a n_z-\beta w & \beta & \phi\\ \tilde{\gamma}_r+\tilde{U}a & -a n_x-\beta u & -a n_y-\beta v & -a n_z-\beta w & \beta & \phi\\ -e_V\tilde{\gamma}_r & \beta u e_V & \beta v e_V & \beta w e_V & -\beta e_V & a^2-\phi e_V\end{bmatrix}$$

$$L=\begin{bmatrix}\delta_{sr}/a^2 & 0 & 0 & c_s/2a^2 & c_s/2a^2 & 0\\ u/a^2 & l_x & m_x & (u+a n_x)/2a^2 & (u-a n_x)/2a^2 & 0\\ v/a^2 & l_y & m_y & (v+a n_y)/2a^2 & (v-a n_y)/2a^2 & 0\\ w/a^2 & l_z & m_z & (w+a n_z)/2a^2 & (w-a n_z)/2a^2 & 0\\ \left[\beta(u^2+v^2+w^2)-\tilde{\gamma}_r\right]/\beta a^2 & \tilde{V} & \tilde{W} & (H+a\tilde{U})/2a^2 & (H-a\tilde{U})/2a^2 & -\phi/\beta a^2\\ 0 & 0 & 0 & e_V/2a^2 & e_V/2a^2 & 1/a^2\end{bmatrix}$$

The eigenvalues of Jacobian matrix (43) are

$$\lambda_{1,2,5}=|\mathrm{k}|\tilde{U} \tag{44}$$

$$\lambda_3=|\mathrm{k}|(\tilde{U}+a) \tag{45}$$

$$\lambda_4=|\mathrm{k}|(\tilde{U}-a) \tag{46}$$

where subscript "s" refers to row s and species s, whereas subscript "r" refers to column r and species r. Both s and r vary from 1 to 5 in the present model. The unit vector n is defined from vector k as

$$\mathrm{n}=(n_x,n_y,n_z)=\frac{(k_1,k_2,k_3)}{|\mathrm{k}|} \tag{47}$$

$\mathrm{l}=\left(l_x,l_y,l_z\right)$ and $\mathrm{m}=\left(m_x,m_y,m_z\right)$ are two unit vectors such that n, l, and m are mutually orthogonal. Furthermore, we have,

$$\tilde{U}=un_x+vn_y+wn_z \tag{48}$$

$$\tilde{V}=ul_x+vl_y+wl_z \tag{49}$$

$$\tilde{W}=um_x+vm_y+wm_z \tag{50}$$

The derivative of pressure respecting to conservative variables comes from

$$dp = \beta(d\rho E - ud\rho u - vd\rho v - wd\rho w) + \phi d\rho e_V + \tilde{\gamma}_s d\rho_s \tag{51}$$

where

$$\beta = \frac{\bar{R}}{\rho \sum_s c_s c_{v,tr}^s} \sum_{r=1}^{5} \frac{\rho_r}{M_r} \tag{52}$$

$$\phi = \frac{\bar{R}}{\rho C_{v,V}} \frac{\rho_e}{M_e} - \beta \tag{53}$$

$$\tilde{\gamma}_s = \frac{\bar{R} T_q}{M_s} + \beta \frac{u^2 + v^2 + w^2}{2} - \beta e_s - \phi e_{V,s} \tag{54}$$

$$a^2 = \sum_{s=1}^{5} c_s \tilde{\gamma}_s + \beta \left[H - (u^2 + v^2 + w^2) \right] + \phi e_V = (1 + \beta) \frac{p}{\rho} \tag{55}$$

In equation (54), $T_q = T_V$ when s is an electron, otherwise, $T_q = T$.

In shock-fitting method, the velocity and location of the shock are solved as part of the solutions. The flow variables behind the shock are determined by Rankine-Hugoniot relations across the main shock and a characteristic compatibility relation from behind the shock. For thermochemcial non-equilibrium flow, with the assumptions of "frozen" flow (no chemical reactions and energy relaxations when flow passes through the shock), the species mass fractions and vibration temperature keep constant on the two sides of the shock where translation temperature jumps across the shock. In this way, shock jumps conditions for total density, momentum and total energy are the same as those for perfect gas. In addition, the compatibility relation relating to the maximum eigenvalue in wall normal direction is used. For thermal equilibrium and chemical non-equilibrium flow, only the species mass fractions are assumed to be constant across the shock. The translation and vibration temperatures are jumped simultaneously across the shock. A Newton iteration is used for the jump conditions.

In the interior, compressible Navier-Stokes equations are solved in fully conservative form. An explicit finite difference scheme is used for spatial discretization of the governing equation, the inviscid flux terms are discretized by a fifth-order upwind scheme, and the viscous flux terms are discretized by a sixth-order central scheme. For the inviscid flux vectors, the flux Jacobians contain both positive and negative eigenvalues. A simple local Lax-Friedrichs scheme is used to split vectors into negative and positive wave fields. For example, the flux term F in Eq. (42) can be split into two terms of pure positive and negative eigenvalues as follows

$$F = F_+ + F_- \tag{56}$$

where $F_+ = \frac{1}{2}(F + \lambda U)$ and $F_- = \frac{1}{2}(F - \lambda U)$ and λ is chosen to be larger than the local maximum eigenvalue of F′.

$$\lambda = \frac{|\nabla \eta|}{J} \left(\sqrt{(\varepsilon c)^2 + u'^2} + c \right) \tag{57}$$

where

$$u' = \frac{\eta_x u + \eta_y v + \eta_z w + \eta_t}{|\nabla \eta|} \tag{58}$$

The parameter ε is a small positive constant added to adjust the smoothness of the splitting. The fluxes F_+ and F_- contain only positive and negative eigenvalues respectively. Therefore, in the spatial discretization, the derivative of the flux F is split into two terms

$$\frac{\partial F}{\partial \eta} = \frac{\partial F_+}{\partial \eta} + \frac{\partial F_-}{\partial \eta} \tag{59}$$

where the first term on the right hand side is discretized by the upwind scheme and the second term by the downwind scheme.

The fifth-order explicit scheme utilizes a 7-point stencil and has an adjustable parameter α as follows

$$u_i' = \frac{1}{hb_i}\sum_{k=-3}^{3} a_{i+k}u_{i+k} - \frac{\alpha}{6!b_i}h^5\left(\frac{\partial^6 u}{\partial x^6}\right)_i + \ldots \tag{60}$$

where $\alpha_{i\pm3} = \pm 1 + \frac{1}{12}\alpha,\ \alpha_{i\pm2} = \mp 9 - \frac{1}{2}\alpha,\ \alpha_{i\pm1} = \pm 45 + \frac{5}{4}\alpha,\ \alpha_i = -\frac{5}{3}\alpha$ and $b_i = 60$. The scheme is upwind when α < 0 and downwind when α > 0. It becomes a 6-order central scheme when α = 0 which is used for discretizing viscous terms. All our methods are coded using FORTRAN77 & 90 while Message Passing Interface (MPI) is used for communication in the parallel computations.

3. Models of Wall Blowing-Suction and Regular Porous Coating

In current study, a model of wall blowing-suction disturbance similar to those of Eibler and Bestek [26] is used. The mass flux oscillations on the flat plate within the blowing-suction region can be written as

$$(\rho v)' = q_0 \varepsilon \beta(l) \sin \omega^* t \tag{61}$$

where q_0 is a local constant depending on the location of the blowing-suction actuator, and ε is a small dimensionless parameter representing the amplitude of the mass flux oscillation. The function $\beta(l)$ is the profile function defined within the forcing region as

$$\beta(l) = \begin{cases} 20.25l^5 - 35.4375l^4 + 15.1875l^2 & if \quad 0 \le l \le 1 \\ -20.25(2-l)^5 + 35.4375(2-l)^4 - 15.1875(2-l)^2 & if \quad 1 \le l \le 2 \end{cases} \tag{62}$$

The variable l is a dimensionless coordinate defined within the blowing-suction region,

$$l = \frac{2(x - x_i)}{x_e - x_i} \tag{63}$$

where x_i , x_e are the coordinates of the leading and trailing edges of the blowing-suction actuator. Compared with the sinusoidal profile function in [26], the specific 5th-order-polynomial profile function makes smoother the mass flux oscillations at the edges of the forcing actuator. Due to the anti-symmetric property of the 5th-order-polynomial profile function within the blowing-suction region, the net mass flux introduced to the boundary layer is zero at any instant.

In Eq. (61), ω^* is the circular frequency of single-frequency blowing-suction disturbance, which is related to the frequency by

$$\omega^* = 2\pi f \tag{64}$$

Dimensional circular frequency and frequency are non-dimensionalized as follows,

$$\omega = \frac{\omega^* L}{U_\infty} \tag{65}$$

$$F = \frac{2\pi f \mu_\infty}{\rho_\infty U_\infty^2} = \frac{\omega^* \mu_\infty}{\rho_\infty U_\infty^2} \tag{66}$$

The current studies are focused on linear responses of the boundary layer to forcing waves. In the simulations, the amplitude of mass flux oscillation is small enough to preserve the linear properties of the disturbances. The dimensionless amplitude coefficient, ε in Eq. (61), is given as

$$\varepsilon = 1.0 \times 10^{-5} \tag{67}$$

In the passive control of hypersonic boundary-layer transition by using porous coating, feltmetal coating is initially used [4, 9], because its structure is quite similar to that of the material currently used in thermal protection system. Later, regular coating has been used in most of the researches in this area due to its convenience for parametric studies and new coating design [15, 16]. In the current simulation, regular coatings are modeled by pressure perturbation related wall blowing-suction. The wall blowing-suction induced by porous coating is as follows,

$$v' = A_y p' \tag{68}$$

The porous coating admittance, A_y, is defined as,

$$A_y = -\frac{\phi}{Z_0} \tanh(\Lambda h) \tag{69}$$

In above equation, ϕ is porosity, h is the porous-layer thickness non-dimensionalized by the local length scale of boundary-layer thickness,

$$h = \frac{h^*}{L} = h^* \sqrt{\frac{\rho_\infty U_\infty}{\mu_\infty x}} \tag{70}$$

According to Allard and Champoux's theoretical analyses [27], the empirical equations for porous coating characteristic impedance (Z_0) and propagation constant (Λ) depend on wall temperature, wall density, and edge Mach number of the boundary layer,

$$Z_0 = \frac{\rho_w}{M_e} \sqrt{T_w} \sqrt{\tilde{\rho}/\tilde{C}} \tag{71}$$

$$\Lambda = \frac{i\omega M_e}{\sqrt{T_w}} \sqrt{\tilde{\rho}\tilde{C}} \tag{72}$$

where ρ_w and T_w are the local dimensionless density and temperature on porous surface. The edge Mach number (M_e) is defined right after the shock.

For regular porous coating considered in the current paper, the dynamic density ($\tilde{\rho}$) and the bulk module ($\tilde{C}$) are calculated from the following equations,

$$\tilde{\rho} = -\frac{J_0(k_v)}{J_2(k_v)} \tag{73}$$

$$\tilde{C} = \gamma + (\gamma - 1)\frac{J_2(k_t)}{J_0(k_t)} \tag{74}$$

In above two equations, k_v and k_t are defined as

$$k_v = \sqrt{-\frac{i\omega^* \rho_w r^2}{\mu_w}} \tag{75}$$

$$k_t = k_v \sqrt{\Pr} \tag{76}$$

With the definitions of characteristic impedance and propagation constant, regular coating admittance is generally a complex number. Velocity perturbation calculated by Eq. (68) is also a complex number. However, only the real part of velocity perturbation can be imposed in numerical simulations. The unsteady velocity perturbation in numerical simulation is written relating to the instantaneous pressure perturbation ($p(t^*)$).

$$v(t) = \left|A_y\right| \cos(\varphi) p(t) + \left|A_y\right| \sin(\varphi) \frac{dp(t)}{\omega dt} \tag{77}$$

4. Flow conditions

Freestream flow conditions of the hypersonic boundary-layer flow over a flat plate are the same as those of Hudson's test case [28], i.e.,

$M_\infty = 10$	$T_\infty = 278.0\,\mathrm{K}$	$p_\infty = 4560\,\mathrm{Pa}$
$\Pr = 0.72$	$U_\infty = 3352.3\,\mathrm{m/s}$	$\rho_\infty = 0.056803\,\mathrm{kg/m^3}$
$C_{N_2} = 0.78$	$C_{O_2} = 0.22$	$C_{NO} = 0$
$C_N = 0$	$C_O = 0$	$\bar{M} = 28.79177377\,\mathrm{g/mol}$

For perfect gas flow, $\mathrm{Re}_\infty / L = 10940090.56\ \mathrm{m}^{-1}$. Otherwise, $\mathrm{Re}_\infty / L = 10235487.38\ \mathrm{m}^{-1}$. Here Re_∞ / L is unit Reynolds number defined as

$$\mathrm{Re}_\infty / L = \rho_\infty U_\infty / \mu_\infty \tag{78}$$

The unit Reynolds number of perfect gas flow is larger than that of the other two types of flows, where the transport properties are calculated from collision cross-section area.

The streamwise coordinate along the flat plate can be converted to local Reynolds number by

$$\mathrm{Re}_x = x\,\mathrm{Re}_\infty / L \tag{79}$$

In linear stability theory analysis, Reynolds number based on the local length scale of boundary-layer thickness, L, is generally used. They are expressed as

$$R = \frac{\rho_\infty U_\infty L}{\mu_\infty}, L = \sqrt{\frac{\mu_\infty x}{\rho_\infty U_\infty}} \tag{80}$$

Hence, the relation between R and local Reynolds number Re_x is given by

$$R = \sqrt{\mathrm{Re}_x} \tag{81}$$

With the definitions of Reynolds number R and dimensionless frequency F in Eq. (66), dimensionless circular frequency can also be expressed as

$$\omega = RF \tag{82}$$

In both steady and unsteady simulations, inlet conditions are specified. High-order extrapolation is used for outlet conditions because the flow is hypersonic at the exit except a small region near the flat plate. Flow variables behind the shock are solved by combining Rankine-Hugoniot relations across the shock and a characteristic compatibility relation coming from downstream flow. For steady base flow simulation, the wall is adiabatic, and the physical boundary condition of velocity on flat plate is non-slip condition. In unsteady simulations, special treatment of wall boundary conditions is needed. When wall blowing-suction is introduced, temperature perturbation is set to zero, which is a standard boundary condition for theoretical and numerical studies of high frequency disturbances. Meanwhile, non-slip condition is applied on flat plate except the forcing region. Boundary conditions on regular porous coating are quite similar to that in blowing-suction region.

To study the response of the boundary layer to single-frequency wall blowing-suction, six cases of unsteady simulations are carried out for different frequency. In all cases, blowing-suction disturbances are introduced in the region from $x = 0.075$ m ($R = 905.82$) to $x = 0.085$ m ($R = 964.32$). Figure 6 schematically shows the profile of blowing-suction disturbances defined in Eq. (61). Frequencies of wall blowing-suction for the six cases of simulations are listed in Table 3.

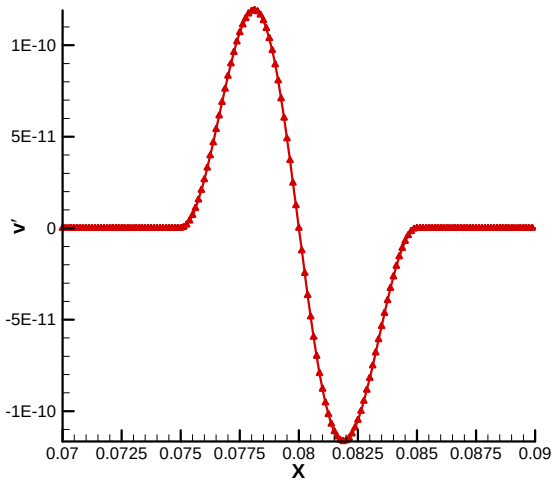

Fig. 6. A schematic of the profile of blowing-suction disturbance.

Table 3. Frequencies of wall blowing-suction for the six cases of simulations

Case #	Frequency, f (kHz)	Frequency, F	Circular frequency, ω at $x = 0.425$ m
1	300	$5.13969398 \times 10^{-5}$	0.11082613434
2	400	$6.85292531 \times 10^{-5}$	0.14776817919
3	500	$8.56615664 \times 10^{-5}$	0.18471022404
4	600	0.00010279388	0.22165226954
5	700	0.000119926193	0.25859431374
6	800	0.000137058506	0.29553635795

5. Result and Discussion

5.1 Steady base flow

In current study, three types of steady base flow are obtained for perfect gas, thermal equilibrium and chemical non-equilibrium gas (thermal equilibrium gas), and thermochemical non-equilibrium gas. The flows are simulated by solving two-dimensional compressible Navier-Stokes equations with a combination of a fifth-order shock-fitting finite difference method and a second-order TVD scheme. In the leading edge region, there exists a singular point at the tip of flat plate, which will introduce numerical instability if the fifth-order shock-fitting method is used. Therefore, a second-order TVD scheme is applied to simulate steady base flow in a small region including the leading edge. For perfect gas flow, the computational domain for the fifth-order shock-fitting method starts at $x = 0.02$ m and ends at $x = 0.435$ m, corresponding to $R = 467.76$ and $R = 2181.50$, respectively. For thermal equilibrium flow and non-equilibrium flow, the computational domains for the fifth-order shock-fitting method start at $x = 0.02$ m and end at $x = 0.20$ m.

In actual simulations of perfect gas flow, the computational domain is divided into six zones with a total of 2081 grid points in streamwise direction. The number of grid points in wall-normal direction is 201. Forty-one points are used in the overlapped region between two neighboring zones, which is proved to be sufficient to make the solution accurate and smooth within the whole domain. An exponential stretching function is used in wall-normal direction to cluster more points inside the boundary layer. On the other hand, the grid points are uniformly distributed in streamwise direction. The grid structures for the other two types of base flow are quite similar.

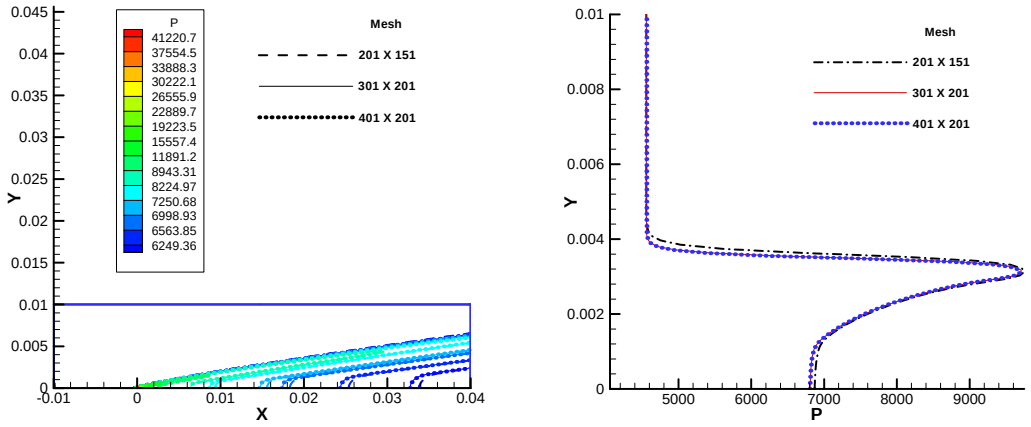

(a) pressure contour

(b) pressure distribution in wall-normal direction at x = 0.02 m.

Fig. 7. Plots of grid convergence study.

For shock-fitting simulation in the first zone, inlet conditions are obtained from the results of shock-capturing simulation in a small region including the leading edge, where a second-order TVD scheme is used to simulate steady base flow. For shock-fitting simulations in other zones, inlet conditions are interpolated from the results of previous zone. Computational domain for shock-capturing simulation starts at $x = -0.01$ m and ends at $x = 0.04$ m ($R = 661.52$). Three sets of grid structures are used to check grid independence of numerical simulation results for perfect gas flow. Figure 7(a) compares pressure contours near the leading edge for three sets of

grid structures. It shows that pressure contours on 301×201 mesh agree well with those on 401×201 mesh, whereas they have significant discrepancies with pressure contours on 201×151 mesh. This figure indicates that the grid structure of 401×201 is fine enough to ensure grid independence of numerical simulation results. However, the grid structure of 201×151 is too coarse to achieve spatially converged results. Similar conclusion can be drawn in Fig. 7(b), where pressure distributions in wall-normal direction are compared. In this figure, pressure distributions are evaluated at $x = 0.02$ m ($R = 467.76$).

Figure 8 shows density contours of steady base flow computed by the fifth-order shock-fitting method for perfect gas flow. After $x = 0.02$ m, the upper boundary of flow field represents bow shock induced by displacement thickness of the boundary layer. The lower boundary is the flat plate. At a fixed location in streamwise direction, pressure behind the shock is higher than that on flat plate due to the existence of bow shock. Figure 9 shows pressure contours of perfect gas solution. It is noticed that pressure is approximately a constant across the boundary layer and along the Mach lines, which is consistent with boundary layer theory and inviscid supersonic aerodynamics. Figures 8 and 9 also show that density and pressure contours have good agreements within the overlap region, which indicates that the TVD solutions are accurate to be used as inlet conditions for the fifth-order shock-fitting simulation in the first zone.

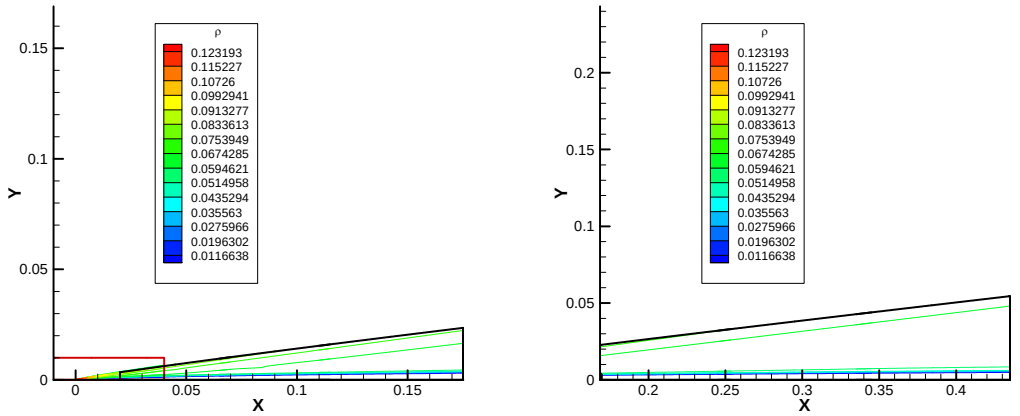

Fig. 8. Density contour of perfect gas solution.

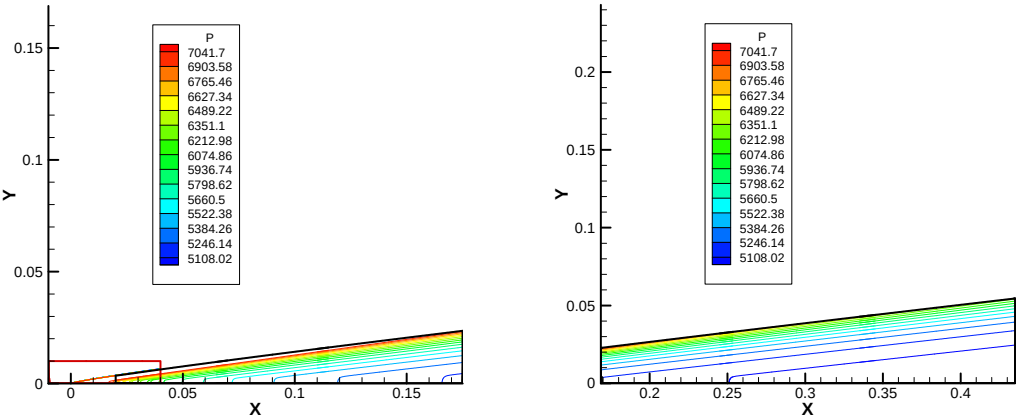

Fig. 9. Pressure contour of perfect gas solution.

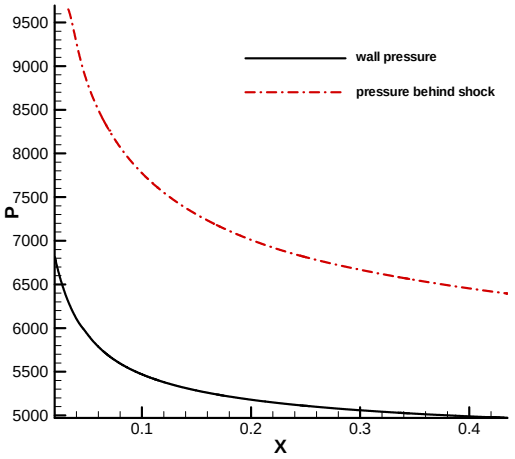

Fig. 10. Distributions of wall pressure and pressure behind shock of perfect gas solution.

Figure 10 shows distributions of wall pressure and pressure behind bow shock computed by the fifth-order shock-fitting method for perfect gas flow. Large pressure gradient near the leading edge is caused by the interaction between viscous boundary layer and inviscid outer flow. From upstream to downstream, viscous-inviscid interaction becomes weaker with bow shock moving away from the boundary layer. As a result, pressure approaches a constant further downstream, and the flow field approaches the self-similar solution. Again, Fig. 10 shows that at a fixed location in the streamwise direction, pressure behind the shock is higher than that on flat plate.

Figures 11 and 12 show the pressure contours of thermal equilibrium gas and thermochemical non-equilibrium gas. Again, pressure contours have good agreements within the overlap region, which indicates that the TVD solutions are accurate to be used as inlet conditions for the fifth-order shock-fitting simulation in the first zone. These figures also show pressure is approximately a constant across the boundary layer and along the Mach lines.

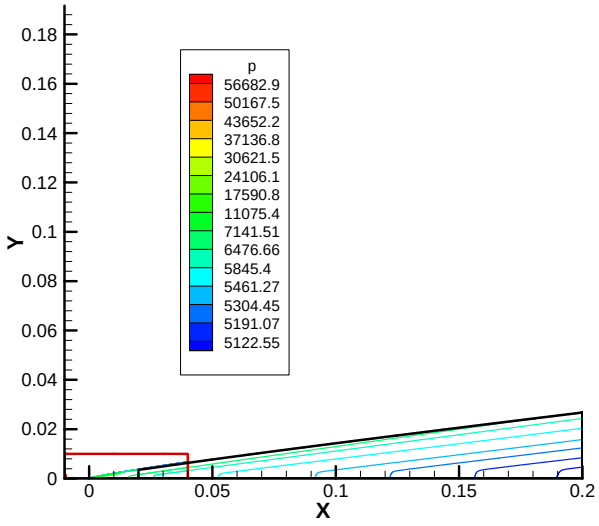

Fig. 11. Pressure contour of thermal equilibrium gas solution.

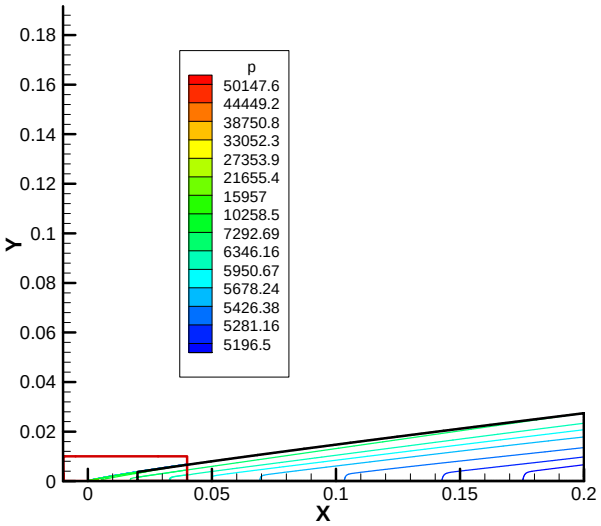

Fig. 12. Pressure contour of thermal equilibrium gas solution.

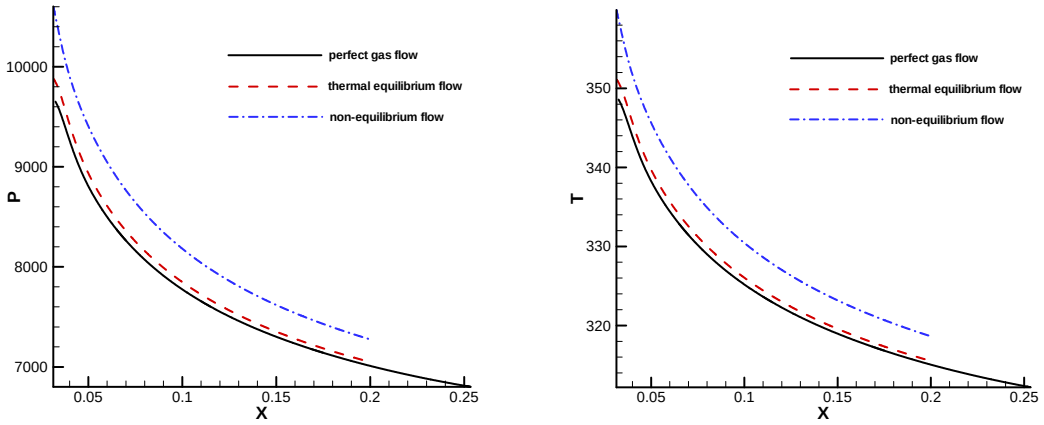

(a) pressure *(b) temperature*

Fig. 13. Distributions of flow variables behind the shock for perfect gas flow, thermal equilibrium flow, and thermochemical non-equilibrium flow.

Figure 13 compares distributions of pressure and translation temperature behind the shock for perfect gas flow, thermal equilibrium flow, and thermochemical non-equilibrium flow. It is clear shown that pressure and translation temperature for thermal equilibrium flow is higher than that of perfect gas flow and is lower than that of non-equilibrium flow. The results indicate that thermal and chemical non-equilibrium effects both increase the pressure and translation temperature behind the shock. Figure 14 shows the shock locations of the three types of steady base flow in the region centered at $x = 0.025$ m ($R = 522.97$). The higher the shock location, the stronger the shock is. The figure shows thermochemical non-equilibrium flow over the flat plate induced the strongest shock. Therefore, the pressure and translation temperature behind the shock is highest for the non-equilibrium flow as shown in Fig. 13.

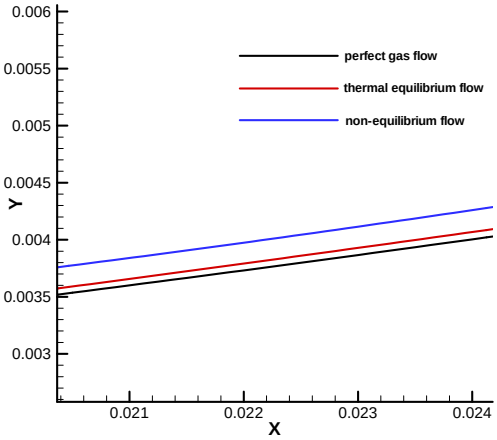

Fig. 14. Comparison of shock locations for perfect gas flow, thermal equilibrium flow, and thermochemical non-equilibrium flow.

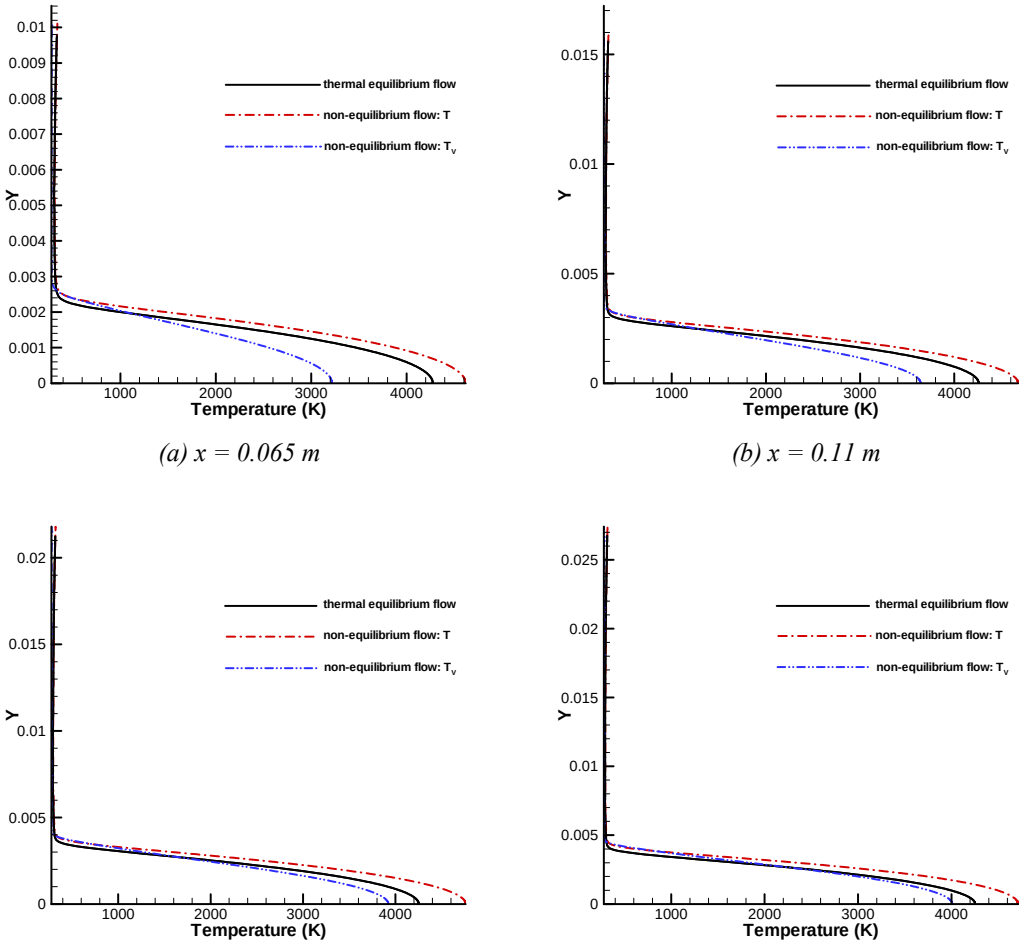

(a) x = 0.065 m

(b) x = 0.11 m

(c) x = 0.155 m

(d) x = 0.2 m

Fig. 15. Comparisons of temperature distributions in wall-normal direction for thermal equilibrium flow and thermochemical non-equilibrium flow.

Figure 15 compares temperature distributions in wall-normal direction for thermal equilibrium flow and non-equilibrium flow at four locations. These figures consistently show that temperature of thermal equilibrium flow is between translation temperature and vibration temperature of non-equilibrium flow. For non-equilibrium flow, the difference between the two temperatures decreases from upstream to downstream.

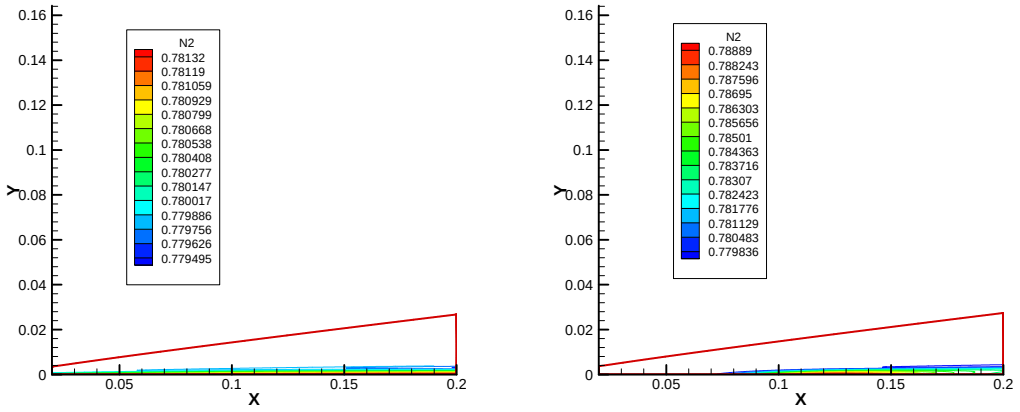

Fig. 16. Comparisons of N2 mass fraction for thermal equilibrium flow and non-equilibrium flow.

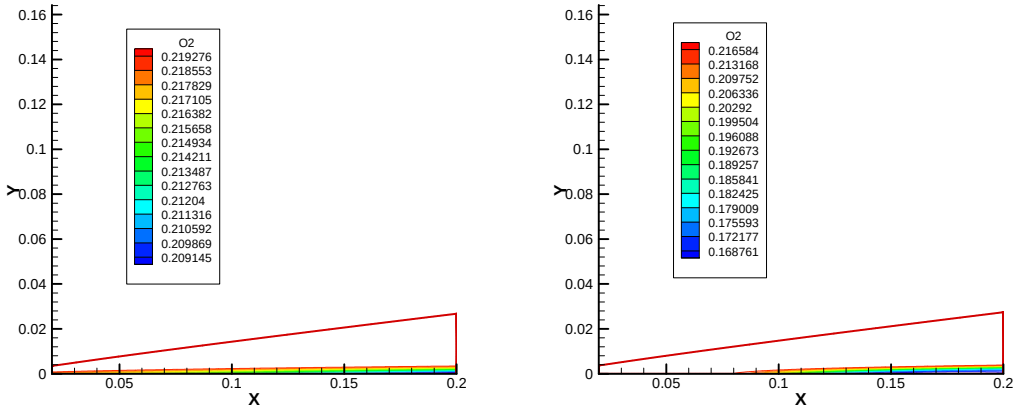

Fig. 17. Comparisons of O2 mass fraction for thermal equilibrium flow and non-equilibrium flow.

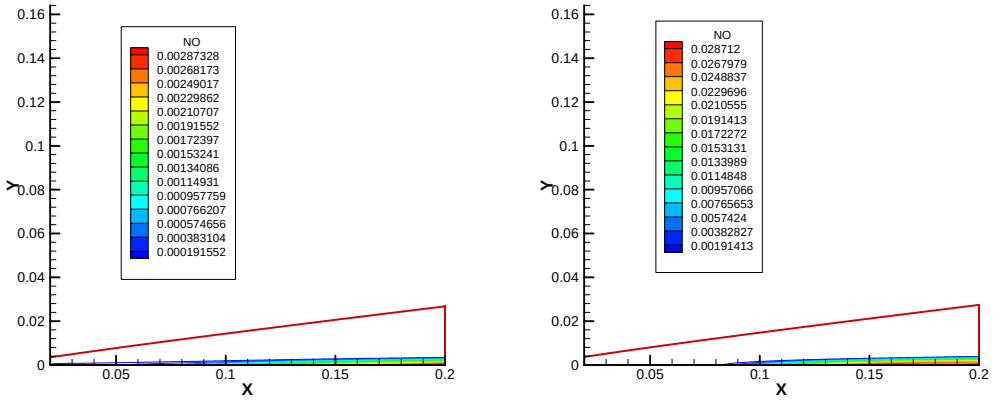

Fig. 18. Comparisons of NO mass fraction for thermal equilibrium flow and non-equilibrium flow.

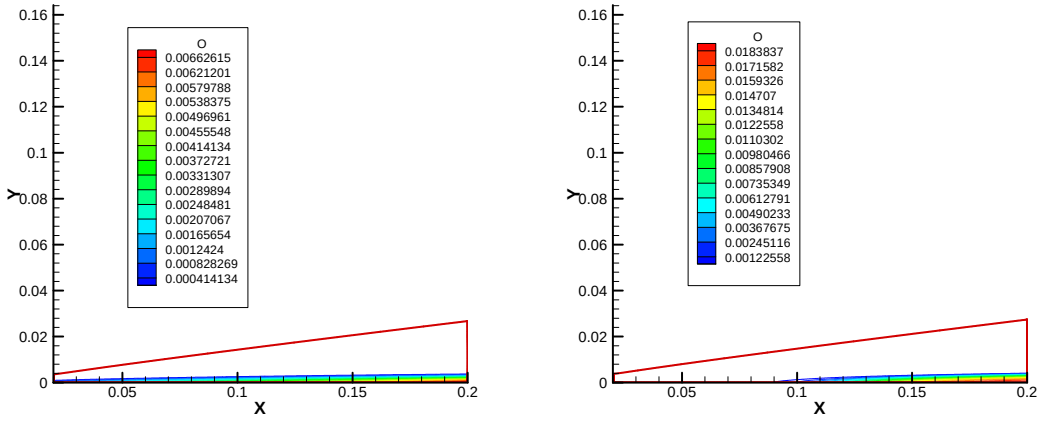

Fig. 19. Comparisons of N2 mass fraction for thermal equilibrium flow and non-equilibrium flow.

Figures 16 to 19 compare species mass fraction for thermal equilibrium flow and thermochemical non-equilibrium flow. The comparison of mass fraction of Nitrogen atom is neglected because it is two scales smaller than other species. The quantitative levels of mass fraction contour show that non-equilibrium flow has much stronger Oxygen dissociation but thermal equilibrium flow has stronger Nitrogen dissociation.

5.2 Boundary-layer stability characteristics based on perfect gas flow solution

Stability characteristics of the Mach 10 flat-plate boundary layer is studied by the linear stability theory (LST) using a multi-domain spectral method of Malik [29]. Here the LST analyses are carried out based on perfect gas solution. Velocity, pressure, and temperature disturbances are represented by harmonic waves of the form

$$\begin{Bmatrix} \tilde{u} \\ \tilde{v} \\ \tilde{w} \\ \tilde{p} \\ \tilde{T} \end{Bmatrix} = \begin{Bmatrix} \hat{u}(y) \\ \hat{v}(y) \\ \hat{w}(y) \\ \hat{p}(y) \\ \hat{T}(y) \end{Bmatrix} e^{i(\alpha x+\beta z-\omega t)} \tag{83}$$

The two parameters, α and β, are wave number components in streamwise and spanwise directions, and ω is circular frequency.

For two-dimensional wall perturbations, $\beta = 0$. Substituting disturbances in Eq. (83) and steady base flow into linearized Navier-Stokes equations, an ordinary-differential-equation (ODE) system is obtained, i.e.,

$$\left(A\frac{d^2}{dy^2} + B\frac{d}{dy} + C \right)\phi = 0 \tag{84}$$

where ϕ is disturbance vector defined by $\left\{\hat{u}, \hat{v}, \hat{w}, \hat{p}, \hat{T}\right\}^T$. The coefficient matrices of A, B, and C are given in Malik's paper [29]. In spatial stability analysis, the two parameters, ω and β, are

specified as real numbers. The streamwise wave number, α, is a complex number and solved as the eigenvalue of the ODE system. The complex wave number α can be expressed as

$$\alpha = \alpha_r + i\alpha_i \tag{85}$$

where $-\alpha_i$ is the local growth rate. A boundary-layer wave is unstable when $\alpha_i < 0$ whereas it is stable when $\alpha_i > 0$. The points $\alpha_i = 0$ are called neutral points of a boundary-layer wave. The real part, α_r, is the local wave number which can be used to define local phase velocity:

$$a = \frac{\omega}{\alpha_r} \tag{86}$$

Both wave number and phase velocity can be used to identify a boundary-layer wave.

Steady base flow needed for LST analysis can be obtained either by numerically solving Navier-Stokes equations or by computing a self-similar boundary-layer solution. Numerical simulation result is more accurate than self-similar solution, although it is inconvenient to use for LST analysis at series of locations. Figures 20 to 22 show profiles of streamwise velocity, temperature, and pressure in wall-normal direction at the location of $x = 0.425$ m ($R = 2156.28$).

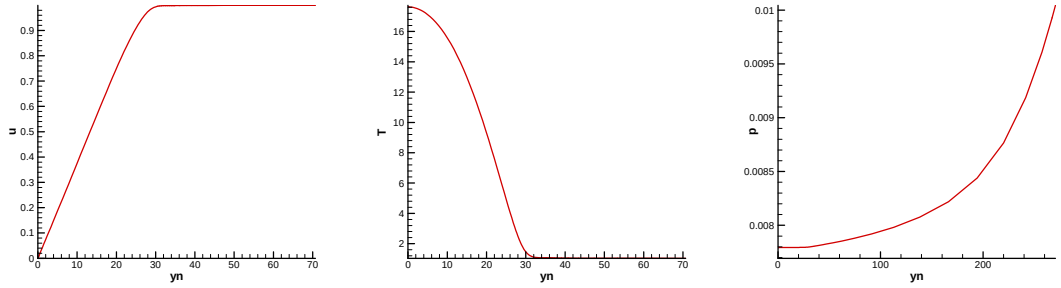

Fig. 20. Profiles of streamwise velocity, temperature, and pressure at x = 0.425 m.

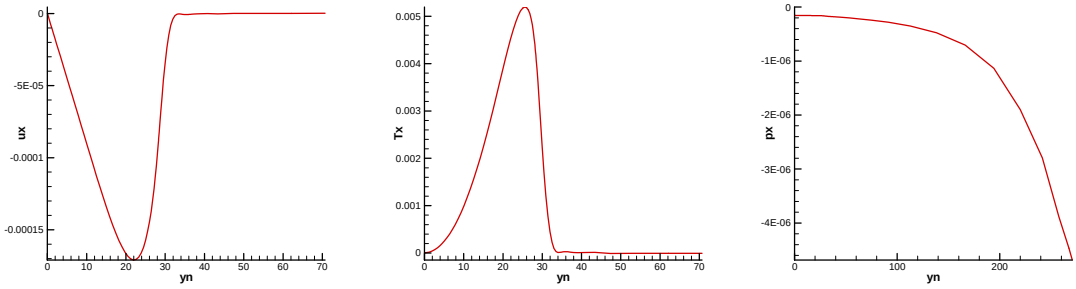

Fig. 21. Streamwise derivatives of streamwise velocity, temperature, and pressure at x = 0.425 m.

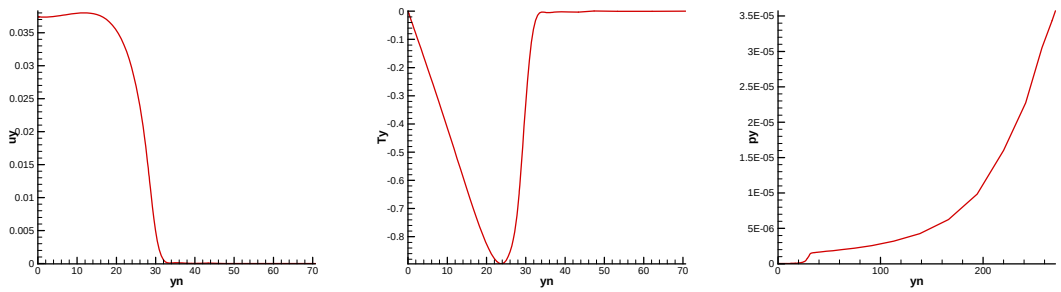

Fig. 22. Wall-normal derivatives of streamwise velocity, temperature, and pressure at x = 0.425 m.

Figure 23 shows dimensionless phase velocities of boundary-layer waves at the location $x = 0.425$ m ($R = 2156.28$) as a function of dimensionless circular frequency. The two horizontal dashed lines represent dimensionless phase velocities of fast acoustic wave ($a = 1 + M_\infty^{-1}$) and slow acoustic wave ($a = 1 + M_\infty^{-1}$). The figure clearly shows that mode F originates from fast acoustic spectrum. As ω increases, phase velocity of mode F decreases. When mode F passes entropy and vorticity spectra near $\omega \approx 0.06$ and $\omega \approx 0.19$, there exists a jump of phase velocity. On the other hand, mode S originates from slow acoustic spectrum. The figure also shows that mode S synchronizes with mode F at the points of ($\omega_s = 0.07062, a_s = 0.95881$) and ($\omega_s = 0.19708, a_s = 0.96881$). The first point is generally called the synchronization point, where mode S and mode F have the same phase velocity and similar eigen-functions (Fig. 24). In this figure, mode S and mode F are identified by their eigen-functions, which are shown in Figs. 24 to 27.

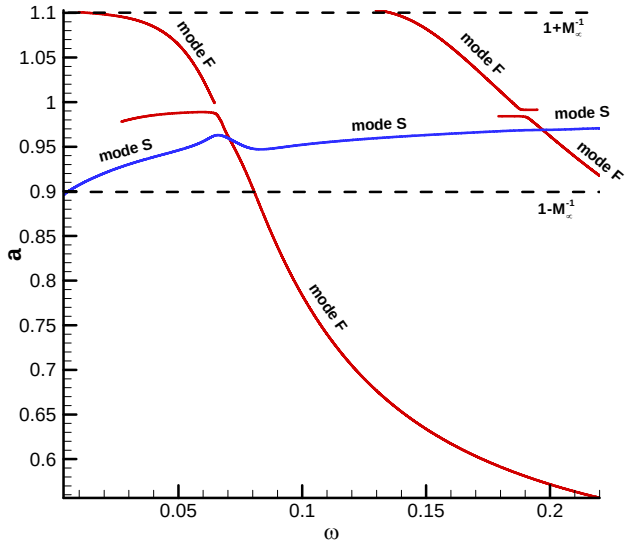

Fig. 23.Distributions of dimensionless phase velocities of boundary-layer waves at x = 0.425 m.

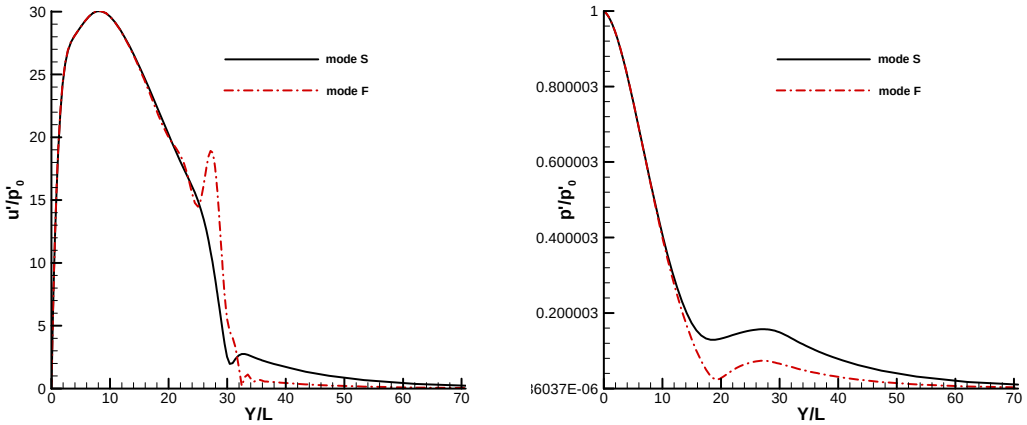

Fig. 24.Eigen-functions of mode S and mode F (lower portion) at ω = 0.07.

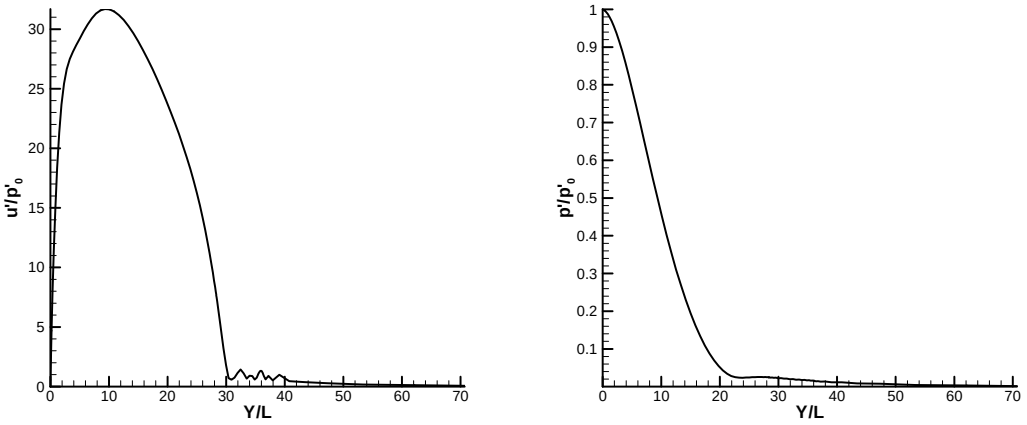

Fig. 25.Eigen-functions of mode F (upper portion) at ω = 0.0646.

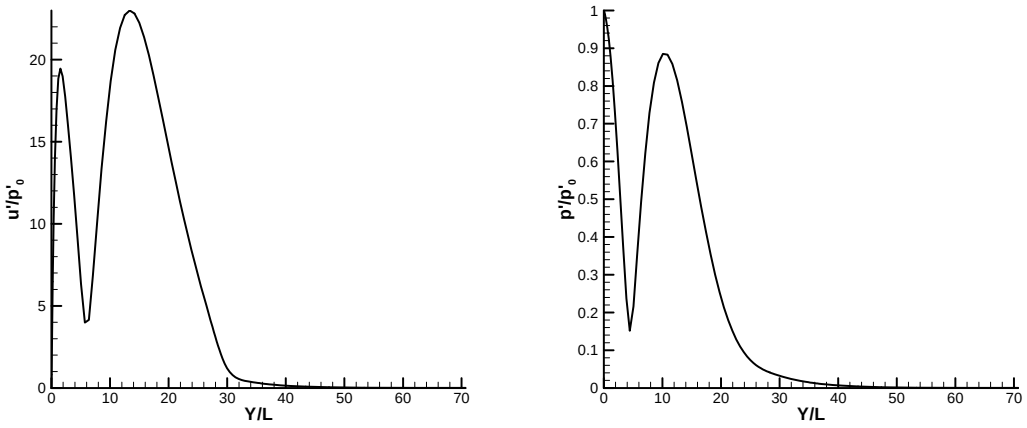

Fig. 26.Eigen-functions of mode F (upper portion) at ω = 0.17.

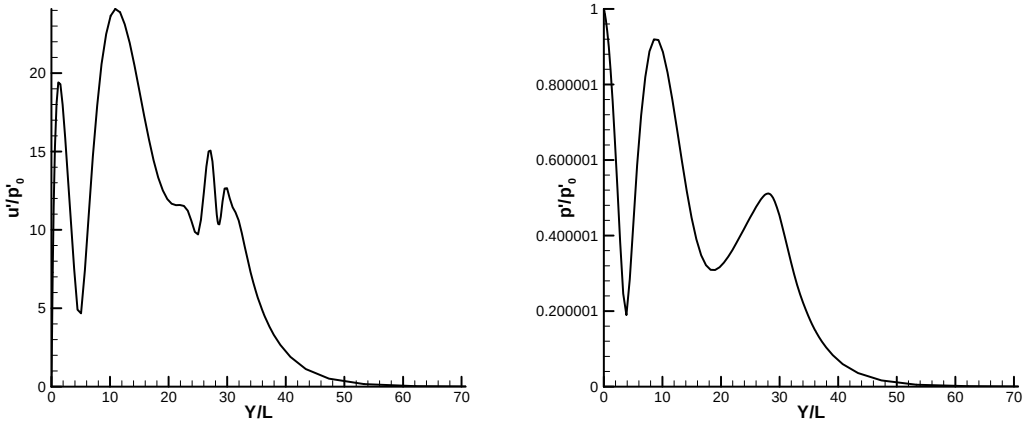

Fig. 27.Eigen-functions of mode S at ω = 0.2.

Figure 28 shows the growth rates of mode F and mode S at $x = 0.425$ m as a function of dimensionless circular frequency. All portions of mode F are stable. Mode S is unstable in a small region around $\omega \approx 0.07$.

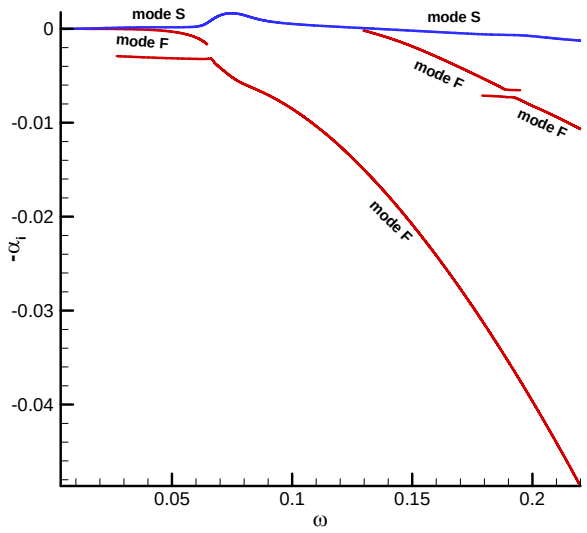

Fig. 28. Distributions of growth rates of mode F and mode S at x = 0.425 m.

According to previous studies [2, 30], the distribution of growth rates are approximately functions of dimensionless frequency only. Therefore, for wall blowing-suction at different frequencies, the growth rates are different with respect to the streamwise coordate x. Figure 29 shows the growth rate of mode S at the six frequencies considered in current paper as listed in Table 3. As the frequency increases from 300 kHz to 800 kHz, the peak of mode S growth rate moves upstream, and mode S becomes unstable earlier. However, the unstable region of mode S shrinks quickly as the frequency increases.

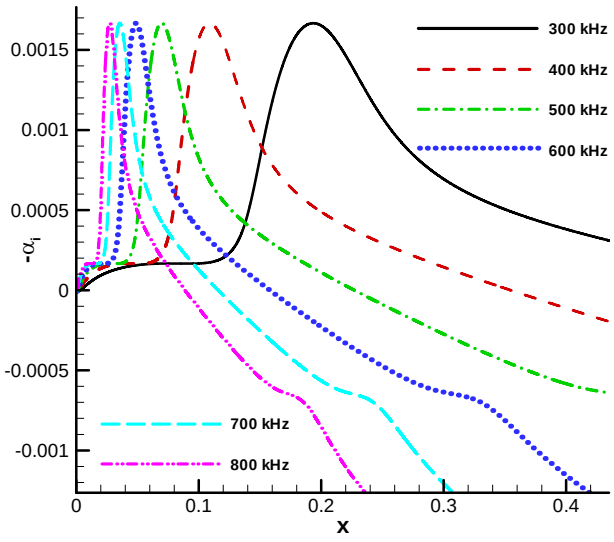

Fig. 29. Distributions of mode S growth rates at different frequencies with respect to x.

5. 3 Response of the boundary layer to single-frequency blowing-suction

The response of the boundary layer to single-frequency to wall blowing-suction is studied by six cases of numerical simulation for perfect gas flow. Since the blowing-suction disturbances are introduced in the region from $x = 0.075$ m to $x = 0.085$ m, it can be expected that the higher frequency blowing-suction will only induce weak boundary-layer waves because mode S becomes stable right after the blowing-suction region.

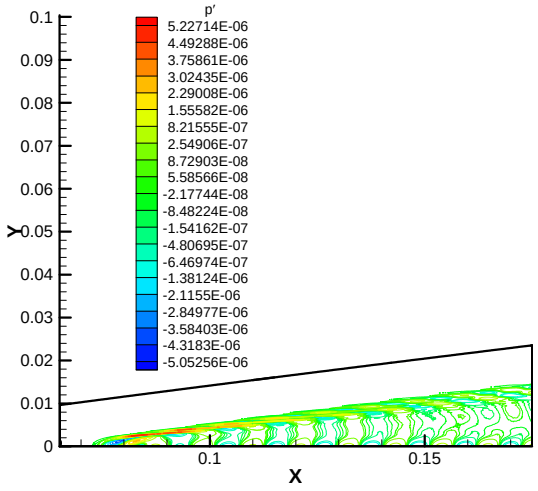

Fig. 30. Instantaneous pressure perturbation excited by blowing-suction at 300 kHz.

Figure 30 shows the instantaneous pressure perturbation field excited by single-frequency wall blowing-suction at the frequency of 300 kHz. Although the strongest pressure perturbations are located outside of the boundary layer and propagating downstream along the Mach lines, there are significant excitation of boundary-layer waves inside the boundary layer. The feature of wave structure inside the boundary layer indicates that mode S (Mack's first mode) is the dominant component. The structure of mode S (Mack's second mode) is observed in Fig. 31, where instantaneous pressure perturbation field excited by wall blowing-suction at 400 kHz is plotted.

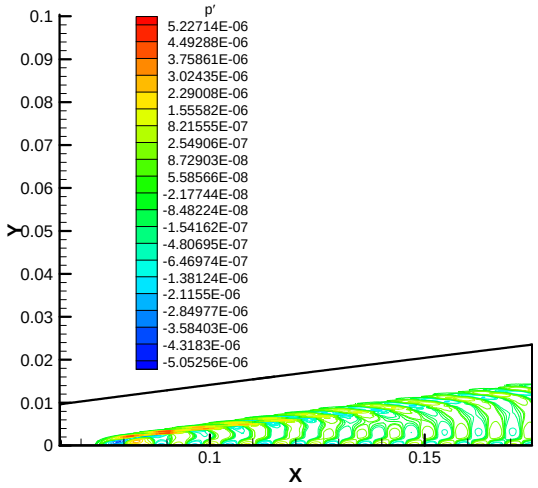

Fig. 31. Instantaneous pressure perturbation excited by blowing-suction at 400 kHz.

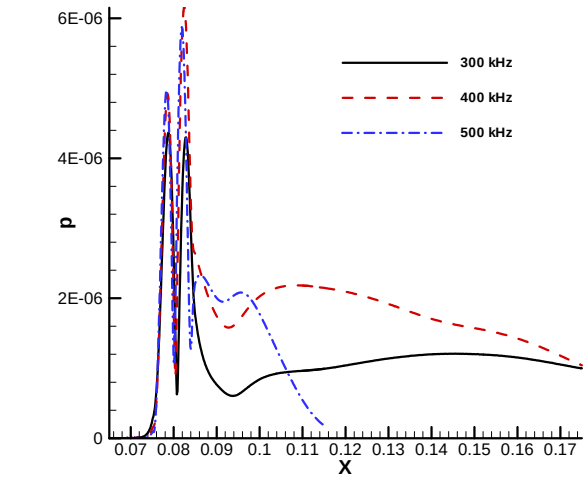

a)

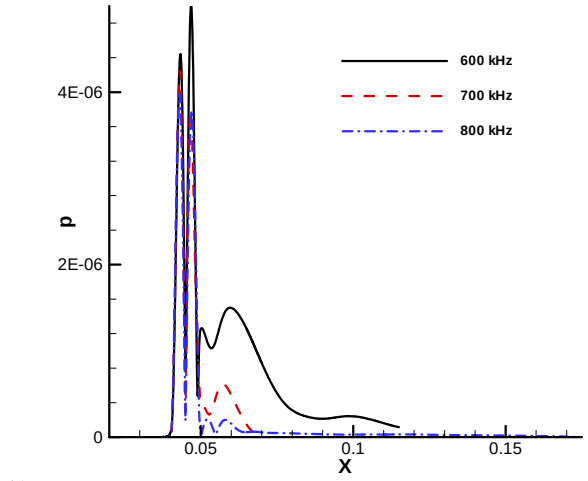

b)

Fig. 32. Distributions of pressure perturbation amplitude along the plate excited by blowing-suction.

Figure 32 compares pressure perturbation amplitudes along the flat plate excited by single-frequency blowing-suction for the six cases of simulations. Since the current simulations are still in the adjacent region of blowing-suction disturbance, there is no enough information to draw quantitative conclusions. But the figure qualitatively shows that the strength of boundary-layer waves generally decreases as the frequency of disturbances increases. The result is consistent with what expected by the LST results. The amplitude of pressure perturbation excited by wall blowing-suction at 400 kHz is the largest because mode S (Mack's second mode) is excited.

5.4 Effect of regular porous coating on boundary-layer waves

As shown in Figs. 30 and 31, mode S is excited in the boundary layer by wall blowing-suction in Cases 3 and 4. New unsteady simulations have been carried out for these two cases by putting

regular porous coating downstream of the blowing-suction region starting at $x = 0.115$ m ($R = 1121.66$). The parameters of regular porous coating are as follows,

$$h^* = 0.45\,\text{mm} \qquad r^* = 25\mu\,\text{m} \qquad \phi = \pi/4$$

Figures 33 and 34 show the instantaneous pressure and wall-normal velocity perturbations along the flat plate for cases 3 and 4. The wall-normal velocity disturbances introduced by regular porous coating are quite small, and their amplitudes closely depend on the instantaneous pressure perturbation.

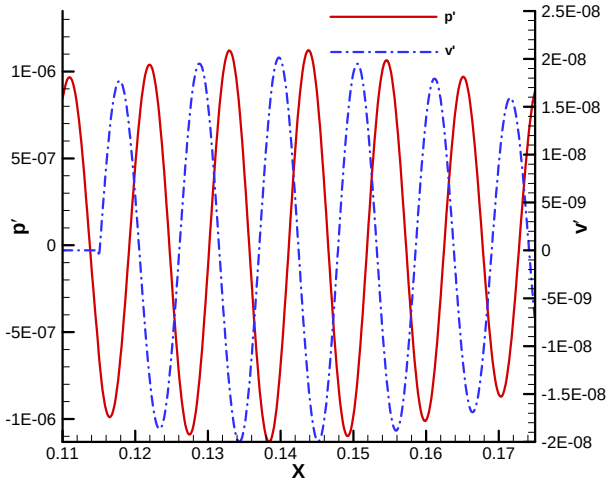

Fig. 33. Instantaneous pressure and wall-normal velocity perturbations along the flat plate for case 3.

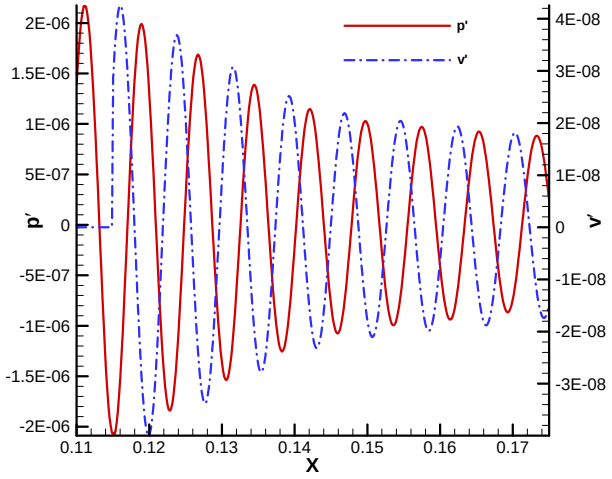

Fig. 34. Instantaneous pressure and wall-normal velocity perturbations along the flat plate for case 4.

Figures 35 and 36 compare pressure perturbation amplitudes along the flat plate for cases 3 and 4 w/ or w/o the effect of regular porous coating. The results show regular porous coating has a significant effect on boundary-layer instability. Boundary-layer waves excited by wall blowing-suction are significantly attenuated by regular porous coating. Such results are consistent with previous studies.

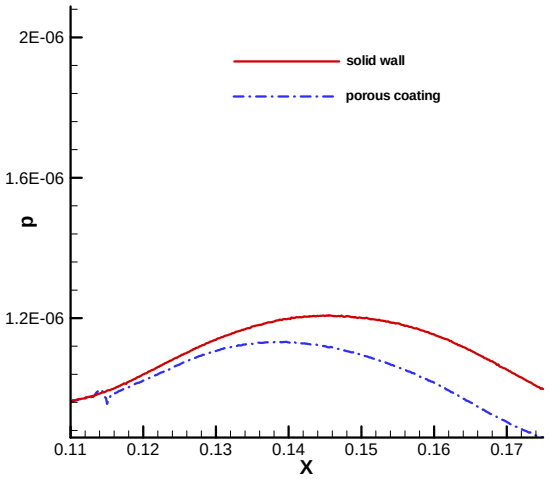

Fig. 35. Comparison of pressure perturbation amplitudes along the flat plate for case 3 w/ or w/o the effect of regular porous coating.

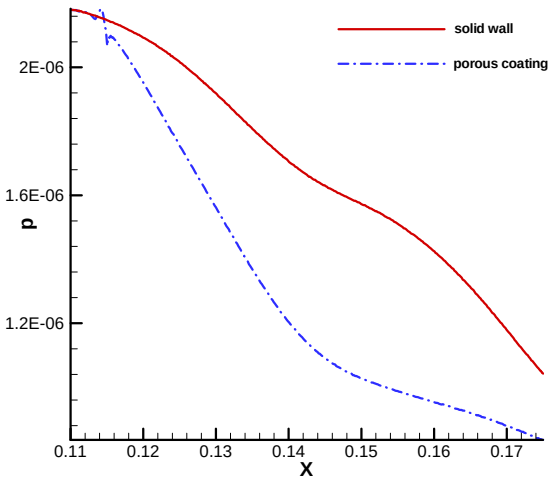

Fig. 36. Comparison of pressure perturbation amplitudes along the flat plate for case 4 w/ or w/o the effect of regular porous coating.

6. Summary

In the current paper, we conduct numerical simulations on the stabilization of a Mach 10 boundary layer using regular porous coating. A high-order shock-fitting non-equilibrium flow solver based on 5-species air chemistry and recent thermal property models is used. The effects of thermochemical non-equilibrium flow including internal energy excitations, translation-vibration energy relaxation, and chemical reactions among different species are considered.

Three types of steady base flow for perfect gas, thermal equilibrium and chemical non-equilibrium gas, and thermochemical non-equilibrium gas are first investigated. For perfect gas flow, the viscosity coefficient is calculated by Sutherland's law and Prandtl number is a given

constant. For the other two types of flow, the transport properties are calculated by collision cross-section area. The results show that thermal and chemical non-equilibrium effects both increase the pressure and translation temperature behind the shock. Furthermore, non-equilibrium flow has much stronger Oxygen dissociation but thermal equilibrium flow has stronger Nitrogen dissociation.

The stability characteristics of the Mach 10 boundary layer are studied by the linear stability theory based on perfect gas solution. Response of the boundary layer to single-frequency wall blowing-suction is studied by six cases of unsteady simulations for perfect gas. The results of unsteady simulations have good agreement with the linear stability theory. The preliminary results show regular porous coating has a significant effect on boundary-layer instability. More steady and unsteady simulations on the passive control of hypersonic non-equilibrium boundary-layer transition using regular porous coating are still ongoing.

Acknowledgments

This work was sponsored by the AFOSR/NASA National Center for Hypersonic Research in Laminar-Turbulent Transition. The views and conclusions contained herein are those of the authors and should not be interpreted as necessarily representing the official policies or endorsements either expressed or implied, of the Air Force Office of Scientific Research, the National Aeronautics and Space Administration, or the U.S. Government.

Reference

1. *Report of the Defense Science Board Task Force on National Aero-Space Plane (NASP) Program*. 1992, Defense Science Board.
2. Zhong, X., and Wang, X., *Direct Numerical Simulation on the Receptivity, Instability, and Transition of Hypersonic Boundary Layers.* Annual Review of Fluid Mechanics, 2012. **44**: p. 527-561.
3. Reshotko, E., *Is Re_θ/Me a meaningful transition criterion?* . AIAA Journal, 2007. **45**(7): p. 1441-1443.
4. Fedorov, A.V., Malmuth, N. D., Rasheed, A., and Hornung, H. G., *Stabilization of hypersonic boundary layers by porous coatings.* AIAA Journal, 2001. **39**(4): p. 605-610.
5. Chokani, N., Bountin, D. A., Shiplyuk, A. N., and Maslov, A. A., *Nonlinear aspects of hypersonic boundary-layer stability on a porous surface.* AIAA Journal, 2005. **43**(1): p. 149-155.
6. Fedorov, A.V., and Malmuth, N. D., *Parametric studies of hypersonic laminar flow control using a porous coating of regular microstructure.* AIAA Paper 2008-588, 2008. .
7. Michael, V., and Stephen, S. O., *Nonlinear stability of hypersonic flow over a cone with passive porous walls.* Journal of Fluid Mechanics, 2012. **713**: p. 528-563.
8. Rasheed, A., Hornung, H. G., Fedorov, A. V., and Malmuth, N. D., *Experiments on passive hypervelocity boundary-layer control using an ultrasonically absorptive surface.* AIAA Journal, 2002. **40**(3): p. 481-489.
9. Fedorov, A.V., Shiplyuk, A. N., Maslov, A. A., Burov, E. V., and Malmuth, N. D., *Stabilization of a hypersonic boundary layer using an ultrasonically absorptive coating.* Journal of Fluid Mechanics, 2003. **479**: p. 99-124.
10. Shiplyuk, A.N., Burov, E. V., Maslov, A. A., and Fomin, V. M., *Effect of porous coatings on stability of hypersonic boundary layers.* Journal of Applied Mechanics and Technical Physics, 2004. **45**(2): p. 286-291.

11. Fedorov, A.V., Kozlov, V. F., Shiplyuk, A. N., Maslov, A. A., and Malmuth, N. D., *Stability of hypersonic boundary layer on porous wall with regular microstructure.* AIAA Journal, 2006. **44**(8): p. 1866-1871.
12. Maslov, A.A., *Stabilization of Hypersonic Boundary Layer by Microstructural Porous Coating.* IUTAM Symposium on One Hundred Years of Boundary Layer Research, 2006.
13. Lukashevich, S.V., Maslov, A. A., Shiplyuk, A. N., Fedorov, A. V., and Soudakov, V. G., *Stabilization of high-speed boundary layer using porous coating of various thickness.* AIAA Paper 2010-4720, 2010.
14. Bres, G.A., and Colonius, T., *Three-dimensional instabilities in compressible flow over open cavities.* Journal of Fluid Mechanics, 2008. **599**: p. 309-339.
15. Egorov, I.V., Fedorov, A. V., and Soudakov, V. G., *Receptivity of a hypersonic boundary layer over a flat plate with a porous coating.* Journal of Fluid Mechanics, 2008. **601**: p. 165-187.
16. Sandham, N.D., and Ludeke, H., *Numerical study of Mach 6 boundary-layer stabilization by means of a porous surface.* AIAA Journal, 2009. **47**(9): p. 2243-2252.
17. Wang, X., and Zhong, X., *The stabilization of a hypersonic boundary layer using local sections of porous coating.* Physics of fluids, 2012. **24**(034105).
18. Wang, X., and Zhong, X., *Passive Control of Hypersonic Boundary-Layer Transition using Regular Porous Coating.* Seventh International Conference on Computational Fluid Dynamics, Paper ICCFD7-1503, 2012.
19. Wang, X., and Zhong, X., *Phase angle of porous coating admittance and its effect on boundary-layer stabilization.* AIAA Paper 2011-3080, 2011.
20. Hash, D., Olejniczak, J, Wright, M. J., Dinish, P., Pulsonetti, M., Hollis, B. R., Gnoffo, P. A., Barnhard, M., Nompelis, I., and Candler, G., *FIRE II Calculations for Hypersonic Nonequilibrium Aerothermodynamics Code Validation: DPLR, LAURA, and US3D*. 2007, AIAA 2007-0605.
21. Gnoffo, P.A., Gupta, R. N., and Shinn, J. L., *Conservation equations and physical models for hypersonic air flows in thermal and chemical nonequilibrium*. 1989, NASA Technical Paper 2867.
22. Candler, G.V., *The computation of weakly ionized hypersonic flows in thermo-chemical nonequilibrium*. 1988, Stanford University.
23. Gupta, R.N., Yos, J. M., Thompson, R. A., and Lee, K-P., *A Review of Reaction Rates and Thermodynamic and Transport Properties for an 11-Species Air Model for Chemical and Thermal Nonequilibrium Calculations to 30 000 K*. 1990, NASA Reference Publication 1232.
24. Park, C., *Nonequilibrium hypersonic aerothermodynamics*. 1990, New York: Wiley. .
25. Zhong, X., *High-order finite-difference schemes for numerical simulation of hypersonic boundary-layer transition.* Journal of Computational Physics, 1998. **144**: p. 662-709.
26. Eibler, W., and Bestek, H., *Spatial numerical simulations of linear and weakly nonlinear instabilities in supersonic boundary layers.* Theoretical and Computational Fluid Dynamics, 1996. **8**: p. 219-235.
27. Allard, J.-F., and Champoux Y., *New empirical equations for sound propagation in rigid frame fibrous materials.* The Journal of the Acoustical Society of America, 1992. **91**(6): p. 3346-3353.
28. Hudson, M.L., Chokani, N., and Candler, G. V., *Linear Stability of Hypersonic Flow in Thermochemical Nonequilibrium.* AIAA Journal, 1997. **35**(6): p. 958-964.
29. Malik, M.R., *Numerical methods for hypersonic boundary layer stability.* Journal of Compuational Physics, 1990. **86**(2): p. 376 - 413.
30. Wang, X., and Zhong, X., *Effect of porous coating on boundary-layer instability.* AIAA Paper 2010-1243, 2010.